



HAL
open science

Spin alignments within the cosmic web: a theory of constrained tidal torques near filaments

Sandrine Codis, Christophe Pichon, Dmitry Pogosyan

► **To cite this version:**

Sandrine Codis, Christophe Pichon, Dmitry Pogosyan. Spin alignments within the cosmic web: a theory of constrained tidal torques near filaments. *Monthly Notices of the Royal Astronomical Society*, 2015, 452, pp.3369-3393. 10.1093/mnras/stv1570 . insu-03644717

HAL Id: insu-03644717

<https://insu.hal.science/insu-03644717>

Submitted on 25 Apr 2022

HAL is a multi-disciplinary open access archive for the deposit and dissemination of scientific research documents, whether they are published or not. The documents may come from teaching and research institutions in France or abroad, or from public or private research centers.

L'archive ouverte pluridisciplinaire **HAL**, est destinée au dépôt et à la diffusion de documents scientifiques de niveau recherche, publiés ou non, émanant des établissements d'enseignement et de recherche français ou étrangers, des laboratoires publics ou privés.

Spin alignments within the cosmic web: a theory of constrained tidal torques near filaments

Sandrine Codis,¹★ Christophe Pichon^{1,2} and Dmitry Pogosyan³

¹*Institut d'Astrophysique de Paris, CNRS & UPMC, UMR 7095, 98 bis Boulevard Arago, F-75014 Paris, France*

²*Institute of Astronomy, University of Cambridge, Madingley Road, Cambridge CB3 0HA, UK*

³*Department of Physics, University of Alberta, 11322-89 Avenue, Edmonton, Alberta T6G 2G7, Canada*

Accepted 2015 July 10. Received 2015 June 28; in original form 2015 April 23

ABSTRACT

The geometry of the cosmic web drives in part the spin acquisition of galaxies. This can be explained in a Lagrangian framework, by identifying the specific long-wavelength correlations within the primordial Gaussian random field (GRF), which are relevant to spin acquisition. Tidal torque theory is revisited in the context of such anisotropic environments, biased by the presence of a filament within a wall. The point process of filament-type saddles represents it most efficiently. The constrained misalignment between the tidal and the inertia tensors in the vicinity of filament-type saddles simply explains the distribution of spin directions. This misalignment implies in particular an *azimuthal* orientation for the spins of more massive galaxies and a spin *alignment* with the filament for less massive galaxies. This prediction is found to be in qualitative agreement with measurements in GRFs and N -body simulations. It relates the transition mass to the geometry of the saddle, and accordingly predicts its measured scaling with the mass of non-linearity. Implications for galaxy formation and weak lensing are briefly discussed, as is the dual theory of spin alignments in walls.

Key words: galaxies: evolution – galaxies: formation – galaxies: kinematics and dynamics – cosmology: theory – large-scale structure of Universe.

1 INTRODUCTION

Modern simulations based on a well-established paradigm of cosmological structure formation predict a significant connection between the geometry and dynamics of the large-scale structure on the one hand, and the evolution of the physical properties of forming galaxies on the other. Key questions formulated decades ago are nevertheless not fully answered. What are the main processes which determine the morphology of galaxies? What is the role played by angular momentum in shaping them?

Pichon et al. (2011) have suggested that the large-scale coherence of the inflow, inherited from the low-density cosmic web, explains why cold flows are so efficient at producing thin high-redshift discs from the inside out (see also Stewart et al. 2013; Prieto et al. 2015; Laigle et al. 2015). On the scale of a given gravitational patch, gas is expelled from adjacent voids, towards sheets and filaments forming at their boundaries. Within these sheets/filaments, the gas shocks and radiatively loses its energy before streaming towards the nodal points of the cosmic network. In the process, it advects angular momentum, hereby seemingly driving the morphology of galaxies (bulge or disc). The evolution of the Hubble sequence in such a scenario is therefore at least in part initially driven by the

geometry of the cosmic web. As a consequence, the distribution of the properties of galaxies measured relative to their cosmic web environment should reflect such a process. In particular, the spin distribution of galaxies should display a preferred mass-dependent orientation relative to the cosmic web.

Both numerical (e.g. Aragón-Calvo et al. 2007; Hahn et al. 2007; Sousbie et al. 2008; Paz, Stasyszyn & Padilla 2008; Zhang et al. 2009; Codis et al. 2012; Libeskind et al. 2013; Aragón-Calvo & Yang 2014; Dubois et al. 2014), and observational evidence (e.g. Tempel et al. 2013) have recently supported this scenario. In parallel, much analytical (e.g. Catelan, Kamionkowski & Blandford 2001; Hirata & Seljak 2004), numerical (e.g. Heavens, Refregier & Heymans 2000; Croft & Metzler 2000; Schneider & Bridle 2010; Schneider, Frenk & Cole 2012; Joachimi et al. 2013b; Codis et al. 2015; Tenneti et al. 2015) and observational (e.g. Brown et al. 2002; Lee & Pen 2002; Bernstein & Norberg 2002; Heymans et al. 2004; Hirata et al. 2004, 2007; Hirata & Seljak 2004; Mandelbaum et al. 2006, 2011; Joachimi et al. 2011, 2013a) efforts have been invested to control the level of intrinsic alignments of galaxies as a potential source of systematic errors in weak gravitational lensing measurements. Such alignments are believed to be a worrisome source of systematics of the future generation of lensing surveys like Euclid or Large Synoptic Survey Telescope. It is therefore of interest to understand from first principles why such intrinsic alignments arise, so as to possibly temper their effects.

* E-mail: codis@iap.fr

Hence we should try and refine a theoretical framework to study the dynamical influence of filaments on galactic scales, via an extension of the peak theory to the truly three-dimensional anisotropic geometry of the circum-galactic medium, and amend the standard galaxy formation model to account for this anisotropy. Towards this end, we will develop here a filament version of an anisotropic ‘peak-background-split’ formalism, i.e. make use of the fact that walls and filaments are the interference patterns of primordial fluctuations on large scales, and induce a corresponding anisotropic boost in overdensity. Indeed, filaments feeding galaxies with cold gas are themselves embedded in larger scale walls imprinting their global geometry (Danovich et al. 2012; Dubois et al. 2012).

On top of these modes, constructive interferences of high-frequency modes produce peaks which thus get a boost in density that allows them to pass the critical threshold necessary to decouple from the overall expansion of the Universe, as envisioned in the spherical collapse model (Gunn & Gott 1972). This well-known biased clustering effect has been invoked to justify the clustering of galaxies around the nodes of the cosmic web (White, Tully & Davis 1988). It also explains why galaxies form in filaments: in walls alone, the actual density boost is typically not sufficiently large to trigger galaxy formation. The main nodes of the cosmic web are where galaxies migrate, not where they form. They thus inherit the anisotropy of their birth place as spin orientation. During migration, they may collide with other galaxies/haloes and erase part of their birth heritage when converting orbital momentum into spin via merger (e.g. Codis et al. 2012). Tidal torque theory should therefore be revisited to account for the anisotropy of this filamentary environment on various scales in order to model primordial and secondary spin acquisition.

In this paper, we will quantify and model the intrinsically 3D geometry of galactic spins while accounting for the geometry of saddle points of the density field. Indeed, saddle points define an anisotropic *point process* which accounts for the presence of filaments embedded in walls (Pogosyan et al. 1998), two critical ingredients in shaping the spins of galaxies.

Taking them into account will in particular allow us to predict the biased geometry of the tidal field in the vicinity of saddle points. This can be formalized using the two-point joint probability of the gravitational potential field and its first to fourth derivatives and imposing a saddle-point constraint. For Gaussian (or quasi-Gaussian) fields these two-point functions are within reach from first principle (Bardeen et al. 1986). A proper account of the anisotropy of the environment in this context will allow us to demonstrate why the spin of the forming galaxies field are first aligned with the filament’s direction.

We will also show that massive galaxies will have their spin preferentially along the azimuthal direction. While relying on a straightforward extension of Press–Schechter’s theory, we will predict the corresponding transition mass’ scaling with the (redshift-dependent) mass of non-linearity, while relying on the so-called cloud-in-cloud problem applied to the filament-background split.

The paper is organized as follows. Section 2 qualitatively presents the basis of the physical process at work in aligning the spin of dark haloes relative to the cosmic web. Section 3 then presents the expected Lagrangian spin distribution near filaments, assuming cylindrical symmetry, and explains the observed mass transition while carrying a multiscale analysis of the fate of collapsing haloes in the vicinity of 2D saddle points. Section 4 revisits this distribution in three dimensions for realistic typical 3D saddle points. Section 5 investigates the predictions of the theory using Gaussian random field (GRF) and N -body simulations, while we finally conclude in

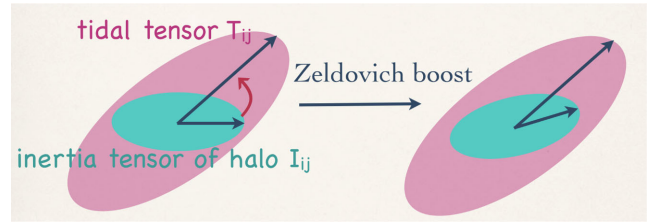


Figure 1. Spin acquisition by tidal torquing. At linear order, the misalignment between the inertia tensor of the proto-object and the surrounding tidal tensor induces an inhomogeneous Zel’dovich boost which corresponds to the acquisition of a net intrinsic angular momentum in Eulerian space.

Section 6. Appendix A discusses possible limitations and extensions of this work. Appendix B presents the dual theory for spin alignment near wall saddles. Finally, Appendix C gathers some technical complements.

2 TIDAL TORQUING NEAR A SADDLE

Before presenting analytical estimates for the expected spins near filament in two and three dimensions and their transition mass, let us discuss qualitatively what underpins the corresponding theory.

2.1 Spin acquisition by tidal torquing

In the standard paradigm of galaxy formation, protogalaxies acquire their spin¹ by tidal torquing coming from the surrounding matter distribution (Hoyle 1949; Peebles 1969; Doroshkevich 1970; White 1984; Catelan & Theuns 1996; Crittenden et al. 2001). At linear order, this spin is acquired gradually until the time of maximal extension (before collapse) and is proportional to the misalignment between the inertia tensor of the protogalaxy and the surrounding tidal tensor (see Schaefer 2009, for a review)

$$L_i = \sum_{j,k,l} a^2(t) \dot{D}_+(t) \epsilon_{ijk} I_{jl} T_{lk}, \quad (1)$$

where $a(t)$ is the scale factor, D_+ the growth factor, T_{ij} the tidal tensor (detraced Hessian of the gravitational potential), I_{ij} the protogalactic inertia tensor (only its traceless part, \bar{I}_{ij} contributes to the spin). As this work focuses on the spin direction, the factor $a^2(t)\dot{D}_+(t)$ will henceforth be dropped for brevity. This process of spin acquisition by tidal torquing is illustrated on Fig. 1.

In the Lagrangian picture, I_{ij} is the moment of inertia of a uniform mass distribution within the Lagrangian image of the halo, while T_{ij} is the tidal tensor averaged within the same image. Thus, to rigorously determine the spin of a halo, one must know the area from which matter is assembled, beyond the spherical approximation. While this can be determined in numerical experiments, theoretically we do not have the knowledge of the exact boundary of a protohalo. As such, one inevitably has to introduce an approximate proxy for the moment of inertia (and an approximation for how the tidal field is averaged over that region).

The most natural approach is to consider that protohaloes form around an elliptical peak in the initial density and approximate its Lagrangian boundary with the elliptical surface where the overdensity drops to zero. This leads to the following approximation for the

¹ Note that in this paper we will call interchangeably ‘spin’ or ‘angular momentum’ the intrinsic angular momentum of (proto)haloes.

traceless part of the inertia tensor (e.g. Schäfer & Merkel 2012, see also equations A2–A4)

$$\bar{T}_{ij} = \frac{2}{5} v \sigma_2 M \bar{H}_{ij}^{-1} = \frac{2}{5} v \sigma_2 \frac{M}{\det \mathbf{H}} \tilde{H}_{ij}, \quad (2)$$

where \bar{H}_{ij}^{-1} is the traceless part of the inverse Hessian of the density field, $H_{ij} = \partial_i \partial_j \delta$, v is the overdensity at the peak and M is the mass of the protohalo. In the second form we explicitly presented the inverse Hessian via the (detraced) matrix of the Hessian minors, \tilde{H}_{ij} . While \tilde{H}_{ij} is a simple polynomial in second derivatives of the density, $M/\det \mathbf{H}$ is not, which is the source of most technical difficulties when statistical studies of the spin are attempted.

Let us point at the following considerations to bypass these difficulties. First, the supplementary condition for the halo to be at a peak of the density yields an extra $\det \mathbf{H}$ factor in all statistical measures (see e.g. Bardeen et al. 1986). This factor exactly cancels the determinant in the denominator. Secondly, all quantities in equation (2) are computed after the density field is smoothed at a particular scale R_h which sets the corresponding mass scale. Therefore, it is more appropriate to apply equation (2) to haloes at *fixed* mass M , determined by that smoothing. Hence, we could argue for the proxy $\bar{T}_{ij} \propto v \tilde{H}_{ij}$ for the moment of inertia for haloes of a given fixed mass, where the change in mass is reflected in the corresponding change in the smoothing scale. In two dimensions, we show in Appendix A that this multiscale approximation gives qualitatively the same statistical results as just using H_{ij} as a proxy. While this approximation is relatively simple, since we are only concerned with the direction of the spin, we will now go one step further and use throughout this paper the Hessian as a proxy for the inertia tensor, even in three dimensions. Indeed, I_{ij} , \tilde{H}_{ij} and H_{ij} share the same eigen-directions (Catelan & Theuns 1996; Schäfer & Merkel 2012), so we *define* the spin for the rest of the paper as

$$s_i \equiv \sum_{j,k,l} \epsilon_{ijk} H_{jl} T_{lk}. \quad (3)$$

The vector field s_i is then quadratic in the successive derivatives of the potential: its (possibly constrained) expectation can therefore be computed for GRFs. This approximation is further discussed in Appendix A. Note that equation (3) improves upon simple parametrizations of the mean misalignment between inertia and tidal tensors (see e.g. Lee & Pen 2000; Crittenden et al. 2001) by *ab initio* explicitly taking into account the correlations between both tensors.

2.2 Geometry of the cosmic web

Galaxies are not forming everywhere but preferentially in filaments and nodes which define the so-called cosmic web (Klypin & Shandarin 1993; Bond, Kofman & Pogosyan 1996). The origin of these structures lies in the asymmetries of the initial GRF describing the primordial universe, amplified by gravitational collapse (Zel'dovich 1970). The presence of such large-scale structure (walls, filaments, nodes) induces local preferred directions for both the tidal tensor and the inertia tensor of forming objects which will eventually turn into preferred alignments of the spin w.r.t the cosmic web. It is therefore of interest to understand what is the expected spin direction predicted by equation (3) given the presence of a typical filament nearby. As a filament is typically the field line that joins two maxima of the density field through a filament-type saddle point (where the gradient is null and the density Hessian has two negative eigenvalues), we choose to study in this paper the expected spin direction of proto-objects *in the vicinity of a filament-type saddle point* with a given geometry (which imposes the direction of the

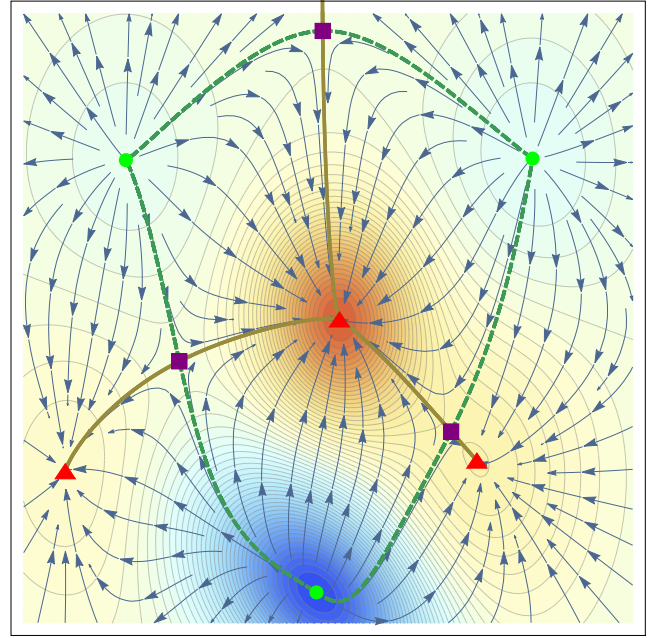


Figure 2. On top of the density contours (from dark blue to dark red), the three (red triangle) maxima (resp. the three (green points) minima) are connected by the crest lines (in solid gold, resp. the through lines in dashed green) which intersect through saddle points (purple squares). The blue arrows represent stream lines of the gradient flow. Throughout this paper, we will assume that the geometry of the regions of intermediate densities are set by the shape of the (purple) saddles.

filament and the wall). Fig. 2 illustrates the geometry of filaments near peaks and saddles in a 2D Gaussian field.

2.3 Constrained tidal torque theory in a nutshell

2.3.1 Spin alignments and flips

It has been shown in simulations (among others Bailin & Steinmetz 2005; Aragón-Calvo et al. 2007; Paz et al. 2008; Zhang et al. 2009; Codis et al. 2012; Libeskind et al. 2013; Forero-Romero, Contreras & Padilla 2014) that the spin of dark haloes is correlated to the direction of the filaments of the cosmic web in a mass-dependent way. The alignment between the spin and the closest filament increases with mass until a mass of maximum alignment (Laigle et al. 2015) that we call here critical mass. As mass increases, the direction of the spin becomes less aligned with the filament before becoming perpendicular to it (Codis et al. 2012). This transition – from aligned to perpendicular – occurs at a mass that we call here the transition mass.

This paper will claim that the critical mass is directly related to the size of the quadrant of coherent angular momentum imposed by the tides of the saddle point (which are effectively the Lagrangian counter parts of the quadrant of vorticity found in Laigle et al. 2015). This mass can be captured using a cylindrical model that would correspond to the plane perpendicular to the filament at the saddle point (which amounts to assuming an infinitely long filament). This 2D toy model (see Section 3 below) shows that near a 2D peak (i.e. near an infinitely long 3D filament), the quadrupolar structure seen in simulation naturally arises in a Lagrangian framework. We investigate the size of that quadrants and shows that it qualitatively predicts the right critical mass.

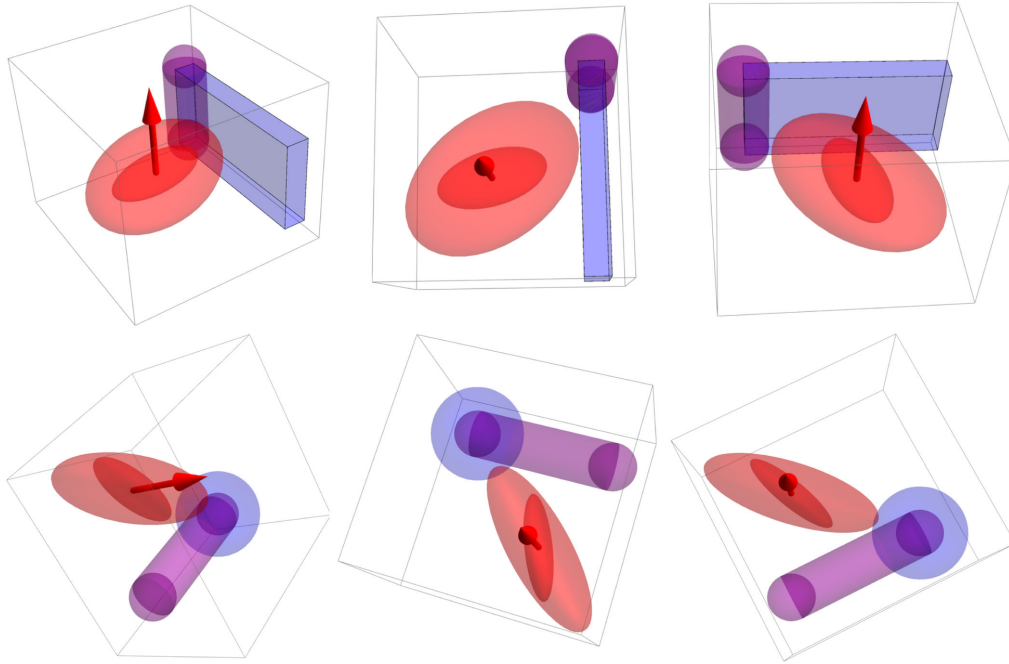


Figure 3. Sketch of main differential alignment between halo shapes and tidal tensor responsible for e_z - and e_ϕ -component of momentum. Top: the two tensors in light and dark red, end up being misaligned as they feel differently the neighbouring wall (blue) and filament (purple), inducing a spin parallel to the filament (red arrow). Three projections are shown for clarity. Bottom: correspondingly, the differential pull from the filament (purple) and the density gradient towards the peak (blue) generates a spin (red arrow) along the azimuthal direction. By symmetry, the other peak(s) on the other side of the saddle point will spin-up massive haloes in the opposite direction.

The second stage of accretion, that flips the spin of more massive haloes from aligned to perpendicular to the filaments, requires a 3D analysis (see Section 4). It is shown that indeed small haloes that form close to the saddle point, acquire spin along the filaments while more massive haloes that form further from the saddle (i.e. closer to the peaks/nodes) acquire a spin perpendicular to the filaments (while accreting smaller haloes). The transition mass will be predicted as a function of redshift and shown to agree with measurements in simulations.

2.3.2 The premises of anisotropic tidal torque theory

Let us present here an outline of the extension of tidal torque theory (TTT) within the context of a peak (or saddle) background split. Given the anisotropically triaxial saddle constraint, we will argue that the misalignment between the tidal tensor and the Hessian of the density field simply explains the transverse and longitudinal anti-symmetric geometry of angular momentum distribution in their vicinity. It arises because the two tensors probe different scales: given their relative correlation lengths, the Hessian probes more directly its closest neighbourhood, while the tidal field, somewhat larger scales.

Within the plane of the saddle point perpendicular to the filament axis (the mid-plane hereafter), the dominant wall (corresponding to the longer axis of the cross-section of the saddle point) will re-orient more the Hessian than the tidal tensor, which also feels the denser, but typically further away saddle point, see Fig. 3, top panels. This net misalignment will induce a spin perpendicular to that plane, i.e. along the filament. This effect will produce a quadrupolar, anti-symmetric distribution of the longitudinal component of the angular momentum which will be strongest at some four points, not far off-axis. Beyond a couple of correlation lengths away from those four

points, the effect of the tidal field induced by the saddle point will subside, as both tensors become more spherical.

Conversely, in planes containing the filament, e.g. containing the main wall, a similar process will misalign both tensors. This time, the two anisotropic features differentially pulling the tensors are the filament on the one hand, and the density gradient towards the peak on the other. The net effect of the corresponding misalignment will be to also spin-up haloes perpendicular to that plane, along the azimuthal direction, see Fig. 3, bottom panels. By symmetry, the anti-clockwise tidal spin will be generated on the other side of the saddle point.

Hence, the geometry of angular momentum near filament-saddle points is the following: it is aligned with the filament in the median plane (within four anti-symmetric quadrants), and (anti-)aligned with the azimuthal direction away from that plane. The stronger the triaxiality the stronger the amplitude. Conversely, if the saddle point becomes degenerate in one or two directions, the component of the angular momentum in the corresponding direction will vanish. For instance, a saddle point in the middle of a very long filament will only display alignment with that filament axis, with no azimuthal component. For a typical triaxial configuration, two pairs of four points define the loci of maximal longitudinal and azimuthal spin.

2.3.3 Geometry of spin flip

Fig. 4 gives a more quantitative account of the geometry of the tidal field around a given saddle point embedded in a given dominant wall. We consider here the angular momentum distribution near a filament-saddle point, S . It is assumed that the three eigenvalues of the density are such that the filament going through this saddle point is along the vertical axis and that the other two eigenvalues are different, reflecting the presence of a dominant wall, in the Sxz plane,

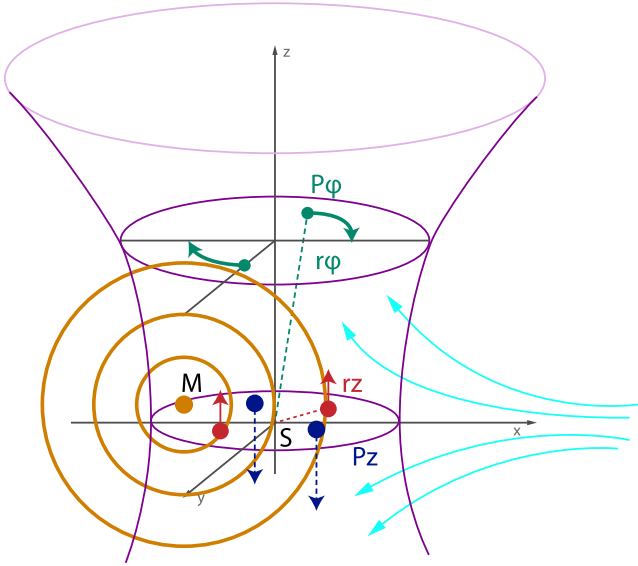


Figure 4. Qualitative geometry of the angular momentum distribution near a elliptical saddle point S (see also Fig. 12). The shape of a given triaxial isodensity is shown in purple, together with two cross-sections, resp. in the Sxy mid-plane and in a plane containing the maxima of transverse angular momentum. The velocity flow in the Sxz plane is shown in cyan. The locus of the Lagrangian extent of haloes is shown in orange concentric spheres centred on M . In the Sxy plane, the four points, P_z correspond to the maxima of the modulus of angular momentum. They point, respectively, along e_z in the first and third quadrants (in red), and along $-e_z$ in the second and fourth quadrant (in blue). Conversely, the four points, P_ϕ , correspond to the maxima of the alignment of s along e_ϕ . Only two (above the mid-plane) are shown. As the orange sphere capture more than one quadrant, the z -component of L subsides, as it encompasses more of the neighbourhood of P_ϕ , and its e_ϕ -component increases. In this Lagrangian framework, the spin flip as a function of mass is a direct consequence of the geometry of the tidal field imposed by the saddle point.

in which the filament is embedded. The shape of a given triaxial isodensity is shown in purple, together with two cross-sections, resp. in the Sxy mid-plane and in a plane containing the maxima of transverse angular momentum. As we will demonstrate later, the spin is mostly confined in the neighbourhood of the Sz -axis, up to a couple of correlation length of the density. It would in fact vanish, should the saddle become isotropic. In the Sxy plane, we identify four quadrants corresponding to regions in which the spin is parallel to the filament. Within these quadrants, the spin point, respectively, along e_z in the first and third quadrants, and along $-e_z$ in the second and fourth quadrants. By symmetry, the spin has to vanish along Sx and Sy .

2.3.4 Towards a transition mass?

The twisted geometry of the spin near the saddle point also allows us to identify the Lagrangian transition mass corresponding to the alignment of dark matter (DM) haloes' spin relative to the direction of their neighbouring filament. Let us first consider the Lagrangian counterpart of a low-mass halo and assume it lies near the median plane. It will typically fall into one of the quadrants corresponding to an orientation of the spin parallel to the filament axis. Now consider a halo of larger Lagrangian extent. As long as its size is smaller than the typical size of a quadrant (which will be defined more precisely below) the alignment increases, until it overextends the quadrant. As it does, two things happen (i) it will start capturing tides from the

next quadrant, which would anti-align it; as the Lagrangian patch radius increases more, it reaches a size comparable to the whole tidal region of influence of the saddle point. It then encompasses both the clockwise and anti-clockwise azimuthal regions, and add up to a net momentum of null amplitude. (ii) it will start capturing the effect of the azimuthal tide, hence inducing a spin flip. Depending on the ratio of the eigenvalues of the Hessian, the two might be concurrent or not. In parallel, as the radius increases, the patch collects the mean potential gradient which defines the Zel'dovich boost which will drive it away from the neighbourhood of the saddle point. The above description clearly accounts for the influence of only one saddle point. As we consider regions further away from that saddle, we should account for the influence of other critical points, as discussed in Section 5.

We have up to now considered a patch centred near the mid-plane close to the saddle point. Indeed, typically, in the peak-background-split framework, such patches will collapse preferentially where the density is boosted, that is within the wall containing the filament, close to the filament. The rarer (more massive) haloes will form in turn in the denser regions, away from the saddle point, along the filament, while the more common lighter haloes will form everywhere and in particular near the saddle point. The former will have a spin perpendicular to the filament. The latter will have a spin parallel to the filament. The relative number of light to small haloes will depend on curvilinear coordinate along the filament because consumption is important: objects above the transition mass have swallowed their lighter parents. At a given redshift, the left overs will decide what matters. This effect is the anisotropic version of the well-known cloud-in-cloud problem.

2.3.5 Lagrangian dynamics of spin flip

In order to understand how a given halo flips, let us split the original Lagrangian patch in two concentric shells. The inner shell will correspond to the Lagrangian extent of the halo as it initially forms, while the outer shell will correspond to secondary infall. The reasoning presented in Section 2.3.2 can be applied independently to both the inner and outer shells, and we would typically conclude that the outer shell would be more likely to have its spin perpendicular to the filament axis. It follows that, as far as this halo is concerned, it will undergo a spin flip as it moves towards the core of the filament and away from the saddle. This process will also correspond to an acquired net helicity for the secondary infall, which will last as long as the transverse anisotropy of the saddle point correlates the local tidal field. In effect, this consistent helicity will build up the spin of the forming galaxy via secondary infall as it drifts, up to the point where mergers will re-orient the direction of its spin. Hence, this constructive build-up of disc should only last so long as the galaxy drifts within the high-helicity region. Note that the transverse motion will correspond to the halo entering the vortex rich caustic corresponding to the multistream region near the filament, so that this Lagrangian description remains fully consistent with the Eulerian discussion given in Laigle et al. (2015). We can anticipate that the longitudinal motion generates azimuthal vortices as well.

The scenario described in this section can be formalized at two levels. First, within the framework of constrained random fields, one can compute the expected geometry of the spin configuration near a given saddle. This will yield a map of the mean alignment between spin and filament in the vicinity of the saddle point. We will then marginalize over the expected distribution of such saddles, and model correspondingly the evolution of the expected mass of

dark haloes around the filament. This will allow us to recover the numerically measured mass transition for spin flip. We may also test the mass-dependent alignment w.r.t. \mathbf{e}_ϕ in GRFs and N -body simulations. For the sake of clarity, we will proceed in two steps: first, while assuming cylindrical symmetry we will compute the expected spin distribution within the most likely cross-section of a filament of infinite extend (Section 3); then we will compute this expectation around the most likely 3D saddle point (Section 4).

3 SPIN ALONG INFINITE FILAMENT

Let us first start while assuming that the filament is of infinite extent, so that we can restrict ourselves to cylindrical symmetry in two dimensions. This is of interest as the angular momentum is then along the filament axis by symmetry and its derivation in the context of TTT is much simpler. It captures already in part the mass transition, in as much as we can define the mean extension of a given quadrant of momentum with a given polarity. In this context, it is of interest to study the spin geometry in the median plane, i.e. in the vicinity of a 2D peak. This 2D spin is along the filament, and will be denoted s_z in what follows.

3.1 Shape of the spin distribution near filaments

Under the assumption that the *direction* of the spin along the z direction is well represented by the fully anti-symmetric (Levi Civita) contraction of the tidal tensor and density Hessian given by equation (3) (e.g. Schäfer & Merkel 2012), it becomes a quadratic function of the second and fourth derivatives of the potential. As such, it becomes possible to compute expectations of it subject to its relative position to a peak with a given geometry (which would correspond to the cross-section of the filament in the mid-plane). Note that, as mentioned in Section 2.1, standard TTT relies, more correctly, on the inertia tensor in place of the Hessian. Even though they have inverse curvature of each other, their set of eigen-directions are locally the same, so we expect the induced spin *direction* – which is the focus of this paper, to be the same, so long as the inertia tensor is well described by its local Taylor expansion.

3.1.1 Constrained joint PDF near peak

Any matrix of second derivatives f_{ij} – rescaled so that $\langle (\Delta f)^2 \rangle = 1$ – can be decomposed into its trace Δf , and its detraced components in the frame of the separation

$$f^+ = (f_{11} - f_{22})/2, \quad f^\times = f_{12}. \quad (4)$$

Then all the correlations between two such matrices, f_{ij} and g_{ij} can be decomposed irreducibly as follows. Let us call $\xi_{fg}^{\Delta\Delta}$, $\xi_{fg}^{\Delta+}$ and $\xi_{fg}^{\times\times}$ the correlation functions in the frame of the separation (which is the first coordinate here) between the second derivatives of the field f and g separated by a distance r :

$$\begin{aligned} \xi_{fg}^{\Delta\Delta}(r) &= \langle \Delta f \Delta g \rangle, \\ \xi_{fg}^{\Delta+}(r) &= \langle \Delta f g^+ \rangle, \\ \xi_{fg}^{\times\times}(r) &= \langle f^\times g^\times \rangle. \end{aligned} \quad (5)$$

All other correlations are trivially expressed in terms of the above as

$$\begin{aligned} \langle f^\times \Delta g \rangle &= 0, \quad \langle f^+ g^\times \rangle = 0, \\ \langle f^+ g^+ \rangle &= \frac{1}{4} \xi_{fg}^{\Delta\Delta}(r) - \xi_{fg}^{\times\times}(r). \end{aligned} \quad (6)$$

Here, we consider two such fields, namely the gravitational potential Φ and the density δ . In the following, these two fields and their first and second derivatives are assumed to be rescaled by their variance $\sigma_0^2 = \langle \Phi^2 \rangle$, $\sigma_1^2 = \langle (\nabla \Phi)^2 \rangle$, $\sigma_2^2 = \langle (\delta = \Delta \Phi)^2 \rangle$, $\sigma_3^2 = \langle (\nabla \delta)^2 \rangle$ and $\sigma_4^2 = \langle (\Delta \delta)^2 \rangle$. The shape parameter of the density field is defined as

$$\gamma = \sigma_3^2 / (\sigma_2 \sigma_4). \quad (7)$$

The rescaled potential and density will be denoted by ϕ and x and the rescaled first and second derivatives by ϕ_i , x_i and ϕ_{ij} , x_{ij} .

Let us gather the first and second derivatives of the gravitational field and the first and second derivatives of the density in a vector denoted by \mathbf{X} spatially located in \mathbf{r}_X and \mathbf{Y} located in \mathbf{r}_Y . The Gaussian joint probability distribution function (PDF) of \mathbf{X} and \mathbf{Y} at the two given locations (\mathbf{r}_X and \mathbf{r}_Y separated by a distance $r = |\mathbf{r}_X - \mathbf{r}_Y|$) obeys

$$\mathcal{P}(\mathbf{X}, \mathbf{Y}) = \frac{1}{\sqrt{\det|2\pi \mathbf{C}|}} \exp\left(-\frac{1}{2} \begin{bmatrix} \mathbf{X} \\ \mathbf{Y} \end{bmatrix}^T \cdot \mathbf{C}^{-1} \cdot \begin{bmatrix} \mathbf{X} \\ \mathbf{Y} \end{bmatrix}\right), \quad (8)$$

where $\mathbf{C}_0 \equiv \langle \mathbf{X} \cdot \mathbf{X}^T \rangle$, $\mathbf{C}_\gamma \equiv \langle \mathbf{X} \cdot \mathbf{Y}^T \rangle$ and

$$\mathbf{C} = \begin{bmatrix} \mathbf{C}_0 & \mathbf{C}_\gamma \\ \mathbf{C}_\gamma^T & \mathbf{C}_0 \end{bmatrix}.$$

All these quantities depend on the separation vector \mathbf{r} only because of statistical homogeneity. This PDF is sufficient to compute the expectation of any quantity involving derivatives of the potential and the density up to second order. All the coefficients can easily be computed from the power spectrum of the potential

$$\begin{aligned} \langle \partial_1^{i_1} \partial_2^{i_2} \phi, \partial_1^{j_1} \partial_2^{j_2} \phi \rangle &= \int_0^\infty \int_0^{2\pi} d\theta dk P_k(k) \exp(ikr \cos \theta) \\ & \quad i^{i_1+i_2} (-i)^{j_1+j_2} (\cos \theta)^{i_1+j_1} (\sin \theta)^{i_2+j_2} \frac{k^{i_1+i_2+j_1+j_2+1}}{\sigma_{i_1+i_2} \sigma_{j_1+j_2}}, \end{aligned} \quad (9)$$

and

$$\sigma_n^2 = \int_0^\infty \int_0^{2\pi} d\theta dk P_k(k) k^{2n+1},$$

where the power spectrum of the potential $P_k(k)$ can include a filter function on a given scale. In this work, we use a Gaussian filter defined in Fourier space by

$$W_G(\mathbf{k}, R) = \frac{1}{(2\pi)^{3/2}} \exp\left(-\frac{k^2 R^2}{2}\right). \quad (10)$$

For instance, the one-point covariance matrix for $(\Delta \phi, \phi^+, \phi^\times, \Delta x, x^+, x^\times)$ at a given point simply reads

$$\mathbf{C}_{02} = \begin{pmatrix} 1 & 0 & 0 & -\gamma & 0 & 0 \\ 0 & 1/8 & 0 & 0 & -\gamma/8 & 0 \\ 0 & 0 & 1/8 & 0 & 0 & -\gamma/8 \\ -\gamma & 0 & 0 & 1 & 0 & 0 \\ 0 & -\gamma/8 & 0 & 0 & 1/8 & 0 \\ 0 & 0 & -\gamma/8 & 0 & 0 & 1/8 \end{pmatrix},$$

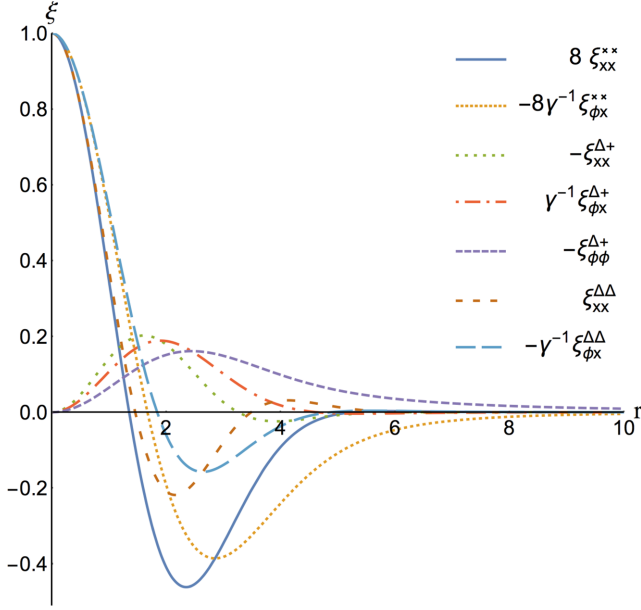


Figure 5. Two-point correlation functions as a function of the separation r in units of the smoothing length for a power-law 2D power spectrum with spectral index $n = -1/2$, i.e. $\gamma = \sqrt{3/7}$. For aesthetic purpose, these functions have been rescaled by their value in $r = 0$ as explicitly written in the legend.

where $\gamma = \sqrt{(n+2)/(n+4)}$ for a scale-invariant density power spectrum with spectral index n (i.e. $n = 4$ for the potential). Note that the first derivatives of the density and the potential fields are decorrelated from the second derivatives meaning that

$$\mathbf{C}_0 = \begin{pmatrix} \mathbf{C}_{01} & 0 \\ 0 & \mathbf{C}_{02} \end{pmatrix},$$

where \mathbf{C}_{01} is the one-point covariance matrix of the gradients of the potential and the density fields $(\phi_1, \phi_2, x_1, x_2)$ as a function of $\gamma' = \sigma_2^2/\sigma_1/\sigma_3$

$$\mathbf{C}_{01} = \begin{pmatrix} 1/2 & 0 & -\gamma'/2 & 0 \\ 0 & 1/2 & 0 & -\gamma'/2 \\ -\gamma'/2 & 0 & 1/2 & 0 \\ 0 & -\gamma'/2 & 0 & 1/2 \end{pmatrix}.$$

The two-point covariance matrix, \mathbf{C}_γ can be similarly derived. In particular, its restriction to the second derivatives of the density and the potential fields can be written as a function of the nine ξ functions defined in equation (5) (for $fg = \phi\phi, \phi x, xx$) (see Fig. 5 and Appendix C2):

$$\begin{pmatrix} \xi_{\phi\phi}^{\Delta\Delta} & \xi_{\phi\phi}^{\Delta+} & 0 & \xi_{\phi x}^{\Delta\Delta} & \xi_{\phi x}^{\Delta+} & 0 \\ \xi_{\phi\phi}^{\Delta+} & \frac{\xi_{\phi\phi}^{\Delta\Delta}}{4} - \xi_{\phi\phi}^{\times\times} & 0 & \xi_{\phi x}^{\Delta+} & \frac{\xi_{\phi x}^{\Delta\Delta}}{4} - \xi_{\phi x}^{\times\times} & 0 \\ 0 & 0 & \xi_{\phi\phi}^{\times\times} & 0 & 0 & \xi_{\phi x}^{\times\times} \\ \xi_{\phi x}^{\Delta\Delta} & \xi_{\phi x}^{\Delta+} & 0 & \xi_{xx}^{\Delta\Delta} & \xi_{xx}^{\Delta+} & 0 \\ \xi_{\phi x}^{\Delta+} & \frac{\xi_{\phi x}^{\Delta\Delta}}{4} - \xi_{\phi x}^{\times\times} & 0 & \xi_{xx}^{\Delta+} & \frac{\xi_{xx}^{\Delta\Delta}}{4} - \xi_{xx}^{\times\times} & 0 \\ 0 & 0 & \xi_{\phi x}^{\times\times} & 0 & 0 & \xi_{xx}^{\times\times} \end{pmatrix}$$

Once the joint PDF given by equation (8) is known, it is straightforward to compute conditional PDFs (in particular subject to a

critical point constraint $\mathcal{C}(\text{crit}) = |\det(x_{ij})| \delta_D(x_i)$). Given the conditionals, simple algebra then yield the conditional density and spin. More specifically, relying on Bayes theorem, the conditional can be expressed in terms of the joint PDF – equation (8) – as

$$\mathcal{P}(X|Y, \text{pk}) = \frac{\mathcal{P}(X, Y, \text{pk})}{\mathcal{P}(Y, \text{pk})},$$

where

$$\mathcal{P}(Y, \text{pk}) = \int dY \mathcal{P}(X, Y) \mathcal{C}(\text{pk})$$

is the marginal distribution describing the likelihood of a given peak, pk (the transverse cross-section of an infinite filament) with a given geometry. Once the conditional, $\mathcal{P}(X|Y, \text{pk})$ is known, it is straightforward² to compute the expectation of any function, $f(X)$ as

$$\langle f(X) | \text{pk} \rangle = \int dX \mathcal{P}(X | \text{pk}) f(X), \quad (11)$$

which, when $f(X)$ is multinomial in the components of X can be carried out analytically. In the following, we will consider in turn functions which are indeed algebraic function of X .

3.1.2 Constrained density maps

From equation (8), given a contrast ν and a geometry for the saddle (or any critical point) defined by $\kappa = \lambda_1 - \lambda_2$, $I_1 = \lambda_1 + \lambda_2$ (where $\lambda_1 > \lambda_2$ are the two eigenvalues of the Hessian of the density field \mathbf{H} – both negative for a peak), the mean density contrast, $\delta_{\text{ext}} = \langle \delta | \text{ext} \rangle$, (in units of σ_2) around the corresponding critical point can be analytically computed

$$\delta(\mathbf{r} | \text{ext}, \kappa, I_1, \nu) = \frac{I_1 (\xi_{\phi x}^{\Delta\Delta} + \gamma \xi_{\phi\phi}^{\Delta\Delta}) + \nu (\xi_{\phi\phi}^{\Delta\Delta} + \gamma \xi_{\phi x}^{\Delta\Delta})}{1 - \gamma^2} + 4(\hat{\mathbf{r}}^T \cdot \overline{\mathbf{H}} \cdot \hat{\mathbf{r}}) \xi_{\phi x}^{\Delta+}, \quad (12)$$

where $\overline{\mathbf{H}}$ is the detraced Hessian of the density and $\hat{\mathbf{r}} = \mathbf{r}/r$ so that

$$\hat{\mathbf{r}}^T \cdot \overline{\mathbf{H}} \cdot \hat{\mathbf{r}} = \kappa \frac{\cos(2\theta)}{2}, \quad (13)$$

r being the distance to the critical point and θ the angle from the eigen-direction corresponding to the first eigenvalue λ_1 of the critical point. When r goes to zero, given the properties of the ξ functions (see Fig. 5), the density trivially converges to the constraint ν .

3.1.3 Constrained 2D spin maps

In two dimensions, the spin is a scalar given by

$$s_z(\mathbf{r}) = \sum_{i,j,k} \epsilon_{ij3} \phi_{ik} x_{jk}, \quad (14)$$

where $\epsilon = \epsilon_{ij3}$ is built upon the totally anti-symmetric rank 3 Levi-Civita tensor ϵ_{ijk} . Since equation (14) is quadratic in the fields x and ϕ , equation (11) can be readily applied to compute analytically its conditional expectation. The angular momentum generated by TTT as a function of the polar position (r, θ) subject to the same critical point constraint at the origin with contrast ν , and principal

² see <http://tinyurl.com/mmbse3z> which describes an implementation in MATHEMATICA of the conditional probability.

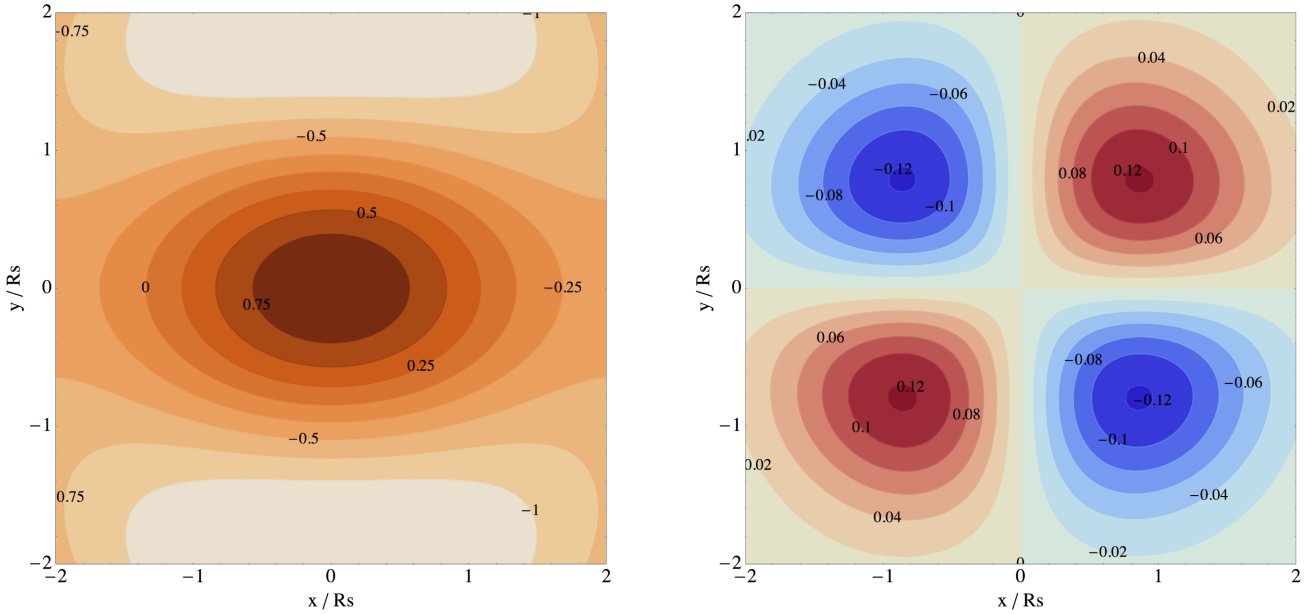


Figure 6. Left: mean density (contrast) field near a 2D peak of height $\nu = 1$, $\lambda_1 = -1$ and $\lambda_2 = -2$ for a power spectrum with index $n = 1/2$ computed from equation (12). Contours are displayed from $\delta = -1$ to 1 by step of $1/4$ as labelled. The x - and y -axes are in units of the smoothing length. Right: corresponding mean spin colour coded from blue (negative) to red (positive) computed from equation (14). The flattening of the filament's cross-section induces a clear quadrupolar spin distribution in its vicinity.

curvatures (λ_1, λ_2) is given by the sum of a quadrupole ($\propto \sin 2\theta$) and an octupole ($\propto \sin 4\theta$)

$$\langle s_z | \text{ext} \rangle = s_z(\mathbf{r} | \text{ext}, \kappa, I_1, \nu),$$

$$= -16(\hat{\mathbf{r}}^T \cdot \boldsymbol{\epsilon} \cdot \overline{\mathbf{H}} \cdot \hat{\mathbf{r}}) (s_z^{(1)} + 2(\hat{\mathbf{r}}^T \cdot \overline{\mathbf{H}} \cdot \hat{\mathbf{r}}) s_z^{(2)}), \quad (15)$$

where the octupolar coefficient $s_z^{(2)}$ can be written as

$$s_z^{(2)}(\mathbf{r}) = (\xi_{\phi x}^{\Delta\Delta} \xi_{xx}^{\times\times} - \xi_{\phi x}^{\times\times} \xi_{xx}^{\Delta\Delta}),$$

and the quadrupolar coefficient $s_z^{(1)}$ reads

$$s_z^{(1)}(\mathbf{r}) = \frac{\nu}{1 - \gamma^2} [(\xi_{\phi\phi}^{\Delta+} + \gamma \xi_{\phi x}^{\Delta+}) \xi_{xx}^{\times\times} - (\xi_{\phi x}^{\Delta+} + \gamma \xi_{xx}^{\Delta+}) \xi_{\phi x}^{\times\times}]$$

$$+ \frac{I_1}{1 - \gamma^2} [(\xi_{\phi x}^{\Delta+} + \gamma \xi_{\phi\phi}^{\Delta+}) \xi_{xx}^{\times\times} - (\xi_{xx}^{\Delta+} + \gamma \xi_{\phi x}^{\Delta+}) \xi_{\phi x}^{\times\times}],$$

while

$$\hat{\mathbf{r}}^T \cdot \boldsymbol{\epsilon} \cdot \overline{\mathbf{H}} \cdot \hat{\mathbf{r}} = -\kappa \frac{\sin(2\theta)}{2}. \quad (16)$$

Equation (15) is remarkably simple. As expected, the spin, s_z , is identically null if the filament is axially symmetric ($\kappa = 0$). It is zero along the principal axis of the Hessian (where $\theta = 0 \bmod \pi/2$ for which $\hat{\mathbf{r}}^T \cdot \boldsymbol{\epsilon} \cdot \hat{\mathbf{r}} = 0$). Near the peak, the anti-symmetric, $\sin(2\theta)$, component dominates, and the spin distribution is quadrupolar. For scale-invariant density power spectra with index n ($n - 4$ for the potential), s_z can be computed explicitly. At small separation, s_z behaves like

$$s_z \propto \kappa((n+2)\nu + \sqrt{(n+2)(n+4)}I_1)r^2 \sin(2\theta), \quad (17)$$

which shows explicitly that the quadrupolar term dominates.

Fig. 6 displays the mean density and spin map for a power-law power spectrum with index $n = 1/2$ around a 2D peak of the density field with geometry $\nu = 1$, $\lambda_1 = -1$ and $\lambda_2 = -2$.

At this stage, it is interesting to understand how much angular momentum is contained into spheres of increasing radius that would feed the forming object at different stages of its evolution. For

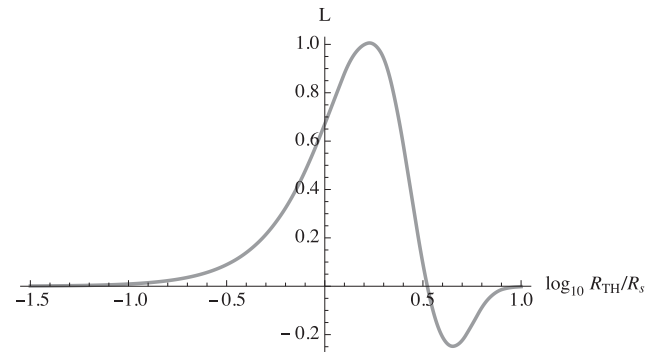


Figure 7. Evolution of the amount of algebraic angular momentum in sphere of radius R_{TH} centred on r_* . The density power-spectrum index is $n = -3/2$, the height of the peak in $(0, 0)$ is $\nu = 1$ and principal curvatures $\lambda_1 = -1$, $\lambda_2 = -2$. The amplitude of the spin is normalized by its maximum value around $R_{\text{TH}} = r_*$.

instance, let us assume there is a small-scale overdensity at (one of the four) location of maximum angular momentum (denoted r_* hereafter) and let us filter the spin field with a top-hat window function centred on r_* and of radius R_{TH} . The resulting amount of angular momentum as a function of this top-hat scale is displayed in Fig. 7. During the first stage of evolution, the central object will acquire spin constructively until it reaches a Lagrangian size of radius $R_{\text{TH}} = r_*$ and feels the two neighbouring quadrants of opposite spin direction. The spin amplitude then decreases and becomes even negative before it is fed by the last quadrant of positive spin. The minimum is reached for radius around $2.4r_*$. This result does not change much with the contrast and the geometry of the peak constraint. Fig. 7 is the Lagrangian counterpart of fig. 4 of Laigle et al. (2015, or fig. 7 of Pichon & Bernardeau 1999) which displays the quadrant of vorticity in the vicinity of filaments.

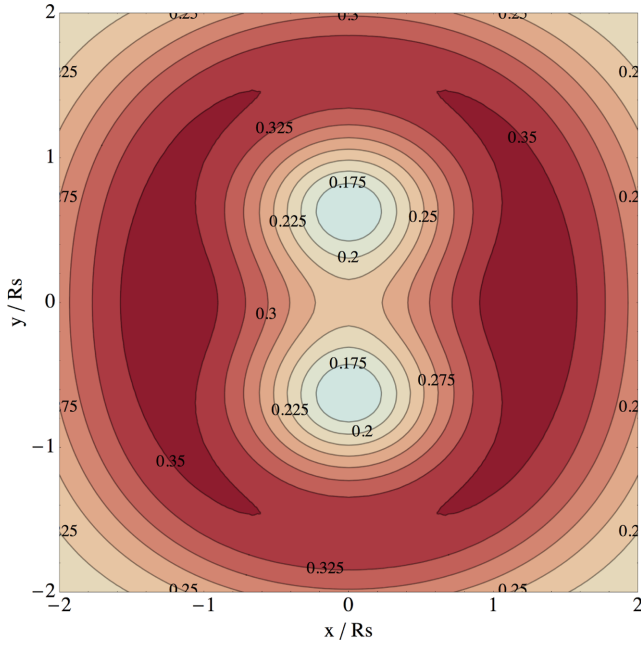


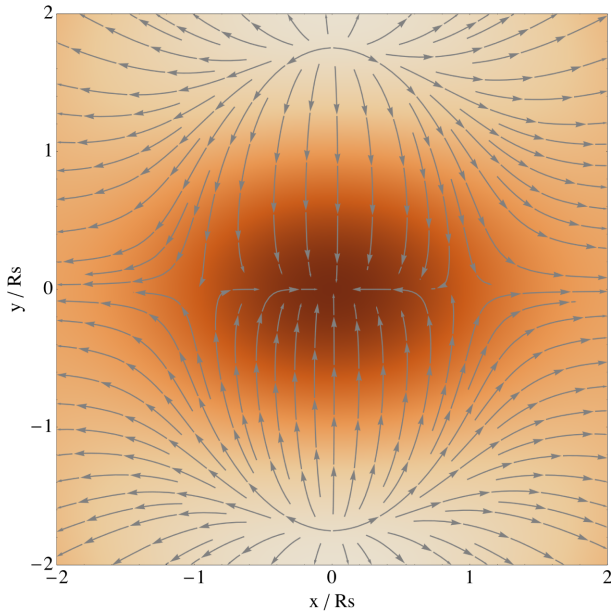
Figure 8. 2D spin dispersion (defined in equation 18) near a 2D peak of height $\nu = 1$ and curvatures $\lambda_1 = -1$ and $\lambda_2 = -2$ for a power spectrum with index $n = 1/2$

3.1.4 Cosmic variance on spin

On top of the mean spin, one can also compute the dispersion of the spin described by

$$\sigma(\mathbf{r}) = \sqrt{\langle s_z^2(\mathbf{r}) \rangle - \langle s_z(\mathbf{r}) \rangle^2}. \quad (18)$$

A map of this spin dispersion is shown on Fig. 8. Comparing Fig. 8 to Fig. 6, we see that spin direction fluctuates along the major axis



of the filament cross-section, and best defined along its minor axis. As the conditional statistics is Gaussian, the whole spin statistics (third moments,...) can in principle be similarly computed.

3.1.5 Zel'dovich mapping of the Spin

Fig. 9 displays the image of the initial density field (resp. initial spin field) translated by a Zel'dovich displacement. The displacement is proportional to (ϕ_1, ϕ_2) here and its expectation given a central peak is trivially computed from the conditional PDFs. The resulting quadrupolar caustics is qualitatively similar to the quadrupolar geometry of the vorticity field measured in numerical simulations (Laigle et al. 2015). Indeed, as discussed in that paper, there is a dual relationship between such Eulerian vorticity maps and the geometry of the spin distribution within the neighbouring patch of a 3D saddle point.

3.2 Transition mass for long filaments

Up to now we assumed that the geometry of the critical point was given. Let us now build the joint statistics of the spin and the mass near 2D peaks.

3.2.1 Geometry of the most likely cross-section

Let us now study what should be the typical geometry of a peak. Following Pogosyan et al. (2009), it is straightforward to derive the PDF for a point to have height ν and geometry κ, I_1 as in their notation $J_2 = \kappa^2$ so that

$$\mathcal{P}(\nu, \kappa, I_1) = \frac{\kappa}{\pi\sqrt{1-\gamma^2}} \exp\left(-\frac{1}{2}\left(\frac{\nu + \gamma I_1}{\sqrt{1-\gamma^2}}\right)^2 - \frac{1}{2}I_1^2 - \kappa^2\right).$$

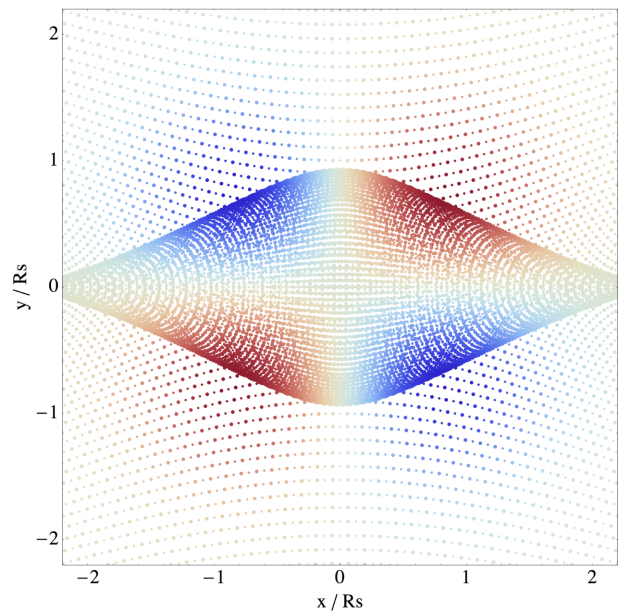


Figure 9. Left: stream lines of the 2D velocity field (defined as the potential gradient) near a 2D peak of height $\nu = 1$ and curvatures $\lambda_1 = -1$ and $\lambda_2 = -2$ for a power spectrum with index $n = 1/2$. Right: Zel'dovich mapping of the spin distribution. There is a good qualitative agreement between the vorticity section presented in Laigle et al. (2015) and this spin map.

Now the PDF for a *peak* to have height ν and geometry κ , I_1 becomes:

$$\mathcal{P}(\nu, \kappa, I_1 | pk) = \frac{\sqrt{3}\kappa|(I_1 - \kappa)(I_1 + \kappa)|}{2\pi\sqrt{1 - \gamma^2}} \Theta(-\kappa - I_1) \times \exp\left(-\frac{1}{2}\left(\frac{\nu + \gamma I_1}{\sqrt{1 - \gamma^2}}\right)^2 - \frac{1}{2}I_1^2 - \kappa^2\right). \quad (19)$$

The maximum of this PDF is trivially reached for $\bar{\nu} = \sqrt{7/3}\gamma$, $\bar{\kappa} = \sqrt{1/3}$ and $\bar{I}_1 = -\sqrt{7/3}$.

3.2.2 The size and area of constant polarity quadrants

From equation (15), it appears clearly that the extension of the region of influence of the critical point is limited, and peaks within each quadrant at some specific (r_*, θ_*) position. Moreover, for small enough κ , the quadrupole dominates, and the extremum is along $\theta = \pi/4$. It is therefore possible to use r_* to define an area in which the spin is significantly non-zero within each quadrant. Let us compute r_* as the radius for which $s_z(\theta = \pi/4)$ is maximal as a function of r .³ The area of a typical quadrant, in which the spin has the same orientation, can then simply be expressed as

$$\mathcal{A} = \pi r_*^2, \quad (20)$$

where $r_* = r_*(\nu, \kappa)$ is the position of a maximum of angular momentum from the peak. Because of the quadrupolar anti-symmetric geometry of the angular momentum distribution near the saddle point, it is typically twice as small (in units of the smoothing length) as one would naively expect.

For power-law density power spectrum with spectral index in the range $n \in] - 2, 2]$, a good fit to its scaling is given by

$$\frac{r_*}{R_s} \approx \frac{3}{250} (n - 5)^2 + \frac{13}{10}, \quad (21)$$

where r_* was computed for the mean geometry given by $\bar{\nu} = \sqrt{7/3}\gamma$, $\bar{\kappa} = \sqrt{1/3}$ and $\bar{I}_1 = -\sqrt{7/3}$.

3.2.3 Critical mass scaling

The critical mass is the mass of maximum spin alignment. In simulation, it has been shown by Laigle et al. (2015) to be $M_{\text{crit}} \approx 10^{12} M_\odot$ at redshift 0. The authors claimed that the critical mass is related to the mass contained in a typical quadrant of vorticity. In this work, we have computed in Lagrangian space the typical area of a quadrant (see equation 20). This area is a function of the smoothing scale. In order to compute it, we need to define a scale. It is reasonable that the maximum spin alignment should be reached for filament that has just collapsed at redshift 0. Indeed, for larger scale filaments, part of the haloes do not lie inside the filament but in the nearby wall which will therefore decrease the mean spin-filament alignment. In previous sections, we focused on $\nu = 0.9$ filaments. The model of the cylindrical collapse then say that those filaments have just collapsed at redshift 0 for a top-hat initial smoothing scale $\sigma(R_{\text{TH}}) = 1.6$ which corresponds to a smoothing length $R_{\text{TH}} = 2.2 \text{ Mpc } h^{-1}$. We can therefore compute the corresponding r_* which is $r_* \approx 1.6R_s \approx 0.7R_{\text{TH}} = 1.5 \text{ Mpc } h^{-1}$ and corresponds to the mass $M_{\text{crit}} = \frac{4}{3}\pi r_*^3 \rho_c \Omega_m \approx 1.5 \cdot 10^{12} M_\odot$, in good

³ Setting $\theta = \pi/4$ effectively neglect the octupolar part of s_z .

agreement with the value measured in simulations. Its redshift evolution is also predicted by the formalism through the cylindrical collapse and could be compared to simulation in future works.

Note that this line of reasoning could be made more rigorous by adding new ingredients in the formalism: a peak constraint at the location of the spin with a smoothing length $R_h < R_s$ so that one can vary R_h (without any assumption on the additivity property of the spin) and see how the spin changes. This formalism can be implemented in two dimensions (see Appendices A2 and A3) and leads to the same order of magnitude for r_* .

4 3D SPIN NEAR AND ALONG FILAMENTS

Let us now turn to the truly three dimensional theory of tidal torques in the vicinity of a typical filament-saddle point. Beyond the obvious increased realism, the main motivation is that the 3D saddle theory fully captures the mass transition.

In three dimensions, we must consider two competing processes. If we vary the radius corresponding to the Lagrangian patch centred on the running point, we have a spin-up (along e_z) arising from the running to wall running to saddle tidal misalignment and a second spin-up (along e_ϕ) arising from running to filament-running peak tidal misalignment. To each position in the vicinity of the central saddle point, we can assign $M(\mathbf{r})$ together with $\cos \mu_z(\mathbf{r})$ and $\cos \mu_\phi(\mathbf{r})$, the cosines of the angle between the spin of the patch and the e_z and e_ϕ direction, respectively. Eliminating \mathbf{r} yields $\cos \mu_z(M)$ and $\cos \mu_\phi(M)$ and therefore yields an estimate of the transition mass.

4.1 Spin distribution along and near filaments

The formalism developed in Section 3 can easily be extended to three dimensions. A critical (saddle) point constraint is now imposed. This critical point is defined by its geometry, namely its height ν and eigenvalues $\lambda_1 \geq \lambda_2 \geq \lambda_3$. Note that such a critical point is a filament-type saddle point if $\lambda_1 \geq 0 \geq \lambda_2 \geq \lambda_3$. In what follows, we decouple the trace from the detraced part of the density Hessian and therefore define the three curvature parameters $I_1 = \lambda_1 + \lambda_2 + \lambda_3$, $\kappa_1 = \lambda_1 - \lambda_2$ and $\kappa_2 = \lambda_2 - \lambda_3$.

4.1.1 Mean density field around a critical point

The resulting mean density (contrast) field subject to that critical point constraint becomes (in units of σ_2):

$$\delta(\mathbf{r} | \text{crit}, I_1, \kappa_1, \kappa_2, \nu) = \frac{I_1 (\xi_{\phi x}^{\Delta\Delta} + \gamma \xi_{\phi\phi}^{\Delta\Delta})}{1 - \gamma^2} + \frac{\nu (\xi_{\phi\phi}^{\Delta\Delta} + \gamma \xi_{\phi x}^{\Delta\Delta})}{1 - \gamma^2} + \frac{15}{2} (\hat{\mathbf{r}}^\top \cdot \bar{\mathbf{H}} \cdot \hat{\mathbf{r}}) \xi_{\phi x}^{\Delta+}, \quad (22)$$

where again $\bar{\mathbf{H}}$ is the detraced Hessian of the density and $\hat{\mathbf{r}} = \mathbf{r}/r$ and we define in 3D $\xi_{\phi x}^{\Delta+}$ as

$$\xi_{\phi x}^{\Delta+} = \langle \Delta x \phi^+ \rangle, \quad (23)$$

with $\phi^+ = \phi_{11} - (\phi_{22} + \phi_{33})/2$. The other ξ functions are defined in the same way as in two dimensions (see equations 5) and displayed on Fig. 10. Note also that $\hat{\mathbf{r}}^\top \cdot \bar{\mathbf{H}} \cdot \hat{\mathbf{r}}$ is a scalar defined explicitly as $\sum_{ij} \hat{r}_i \bar{H}_{ij} \hat{r}_j$. Fig. 11 displays the mean density field around a typical filament-type saddle point. The elongation of the filament along the Oz -axis together with the flattening of the filament in the plane of the wall (Oxz) are clearly visible on this figure.

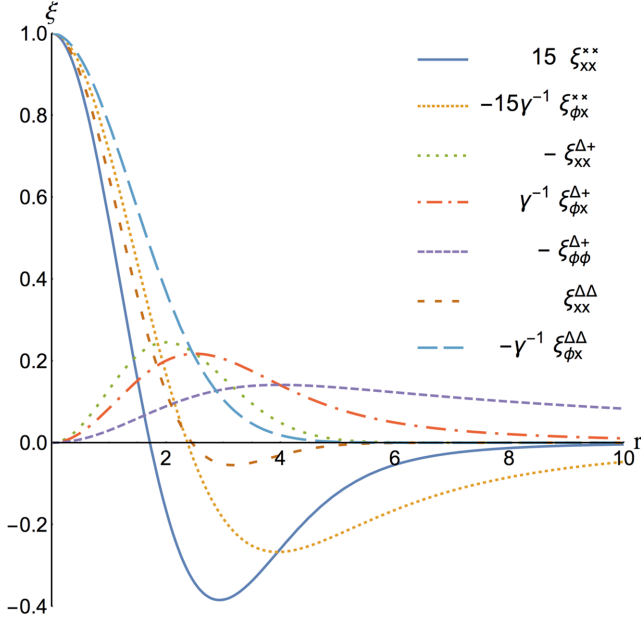


Figure 10. Two-point correlation functions as a function of the separation r in units of the smoothing length for a power-law 3D power spectrum with spectral index $n = -2$, i.e. $\gamma = \sqrt{3}/3$. As in two dimensions, the correlations are rescaled at the origin. See also Fig. C1.

4.1.2 Mean spin field around a critical point

As in two dimensions, the expected spin can also be computed. In three dimensions, the spin, s , is a vector which components are given by

$$s_i = \sum_{j,k,l} \epsilon_{ijk} x_{kl} \phi_{lj}, \quad (24)$$

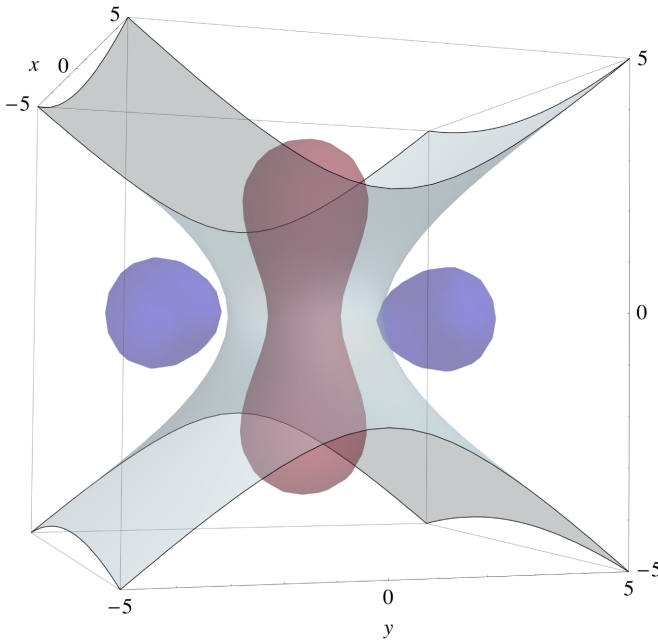


Figure 11. Mean density around a filament-saddle point of height $\nu = 1.25\gamma$, $\lambda_1 = 0.31$, $\lambda_2 = -0.56$, $\lambda_3 = -1$ for a power-law 3D power spectrum with spectral index $n = -2$, i.e. $\gamma = \sqrt{3}/3$. The Ox -, Oy - and Oz -axes are in units of the smoothing length and z is the direction of the filament while the wall is in the plane Oxz . Contours represent the isocontours of the density $\delta = -0.3, 0, 0.5$ from blue to red. A 3D view is displayed on the left-hand panel and a cut in the plane Oyz is shown on the right-hand panel.

with ϵ the rank 3 Levi-Civita tensor. It is found to be orthogonal to the separation and can be written as the sum of two terms

$$s(\mathbf{r}|\text{crit}, I_1, \kappa_1, \kappa_2, \nu) = -15(s^{(1)} + s^{(2)}) \cdot (\hat{\mathbf{r}}^T \cdot \epsilon \cdot \bar{\mathbf{H}} \cdot \hat{\mathbf{r}}), \quad (25)$$

where $s^{(1)}$ is a scalar operator that depends on the height ν and trace of the Hessian I_1

$$s^{(1)} = \left(\frac{\nu}{1-\gamma^2} [(\xi_{\phi\phi}^{\Delta+} + \gamma\xi_{\phi x}^{\Delta+}) \xi_{xx}^{\times\times} - (\xi_{\phi x}^{\Delta+} + \gamma\xi_{xx}^{\Delta+}) \xi_{\phi x}^{\times\times}] \right. \\ \left. + \frac{I_1}{1-\gamma^2} [(\xi_{\phi x}^{\Delta+} + \gamma\xi_{\phi\phi}^{\Delta+}) \xi_{xx}^{\times\times} - (\xi_{xx}^{\Delta+} + \gamma\xi_{\phi x}^{\Delta+}) \xi_{\phi x}^{\times\times}] \right) \mathbb{I}_3,$$

and $s^{(2)}$ a combination of a matricial and a scalar operator that depends on the detraced part of the Hessian

$$s^{(2)} = -\frac{5}{8} \left[2((\xi_{\phi x}^{\Delta+} - \xi_{\phi x}^{\Delta\Delta}) \xi_{xx}^{\times\times} - (\xi_{xx}^{\Delta+} - \xi_{xx}^{\Delta\Delta}) \xi_{\phi x}^{\times\times}) \bar{\mathbf{H}} \right. \\ \left. + ((7\xi_{xx}^{\Delta\Delta} + 5\xi_{\phi x}^{\Delta+}) \xi_{\phi x}^{\times\times} - (7\xi_{\phi x}^{\Delta\Delta} + 5\xi_{\phi x}^{\Delta+}) \xi_{xx}^{\times\times}) \right. \\ \left. \times (\hat{\mathbf{r}}^T \cdot \bar{\mathbf{H}} \cdot \hat{\mathbf{r}}) \mathbb{I}_3 \right]$$

with \mathbb{I}_3 the identity matrix, operating on the vector

$$\hat{\mathbf{r}}^T \cdot \epsilon \cdot \bar{\mathbf{H}} \cdot \hat{\mathbf{r}} = \sum_{ikl} \hat{r}_i \epsilon_{ijk} \bar{H}_{kl} \hat{r}_l. \quad (26)$$

Note that the dependence with the distance r is encoded in the two-point correlation functions, ξ , while the geometry of the critical point is encoded in the terms corresponding to the peak height, trace and detraced part of the Hessian and the orientation of the separation is in $\hat{\mathbf{r}}$. Equation (25) is also remarkably simple: as expected the symmetry of the model induces zero spin along the principal directions of the Hessian (where $\hat{\mathbf{r}}^T \cdot \epsilon \cdot \bar{\mathbf{H}} \cdot \hat{\mathbf{r}} = 0$) and a point reflection symmetry ($\hat{\mathbf{r}} \rightarrow -\hat{\mathbf{r}}$). Note that the correlation functions, ξ can be evaluated for arbitrary power spectra (such as power laws, see Appendix C2, or Λ cold dark matter (Λ CDM), see Appendix C3), hence equation (25) is completely general.

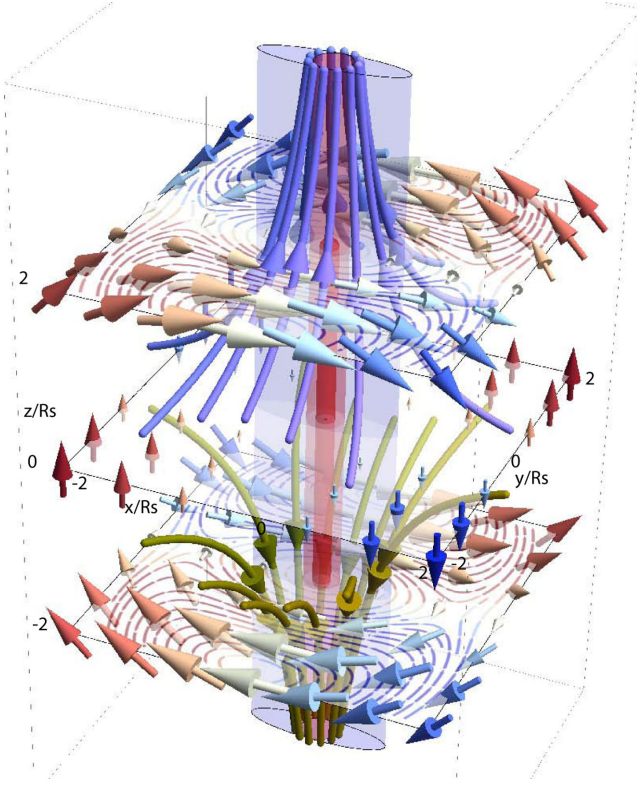


Figure 12. The velocity and spin flow near a vertical filament (in red) embedded in a (purple) wall for $(x, y, z) \in [-2R_s, 2R_s]^3$. The purple and green flow lines trace the (Lagrangian) 3D velocities (upwards and downwards, respectively). The red and blue arrows show the spin 3D distribution, while the three horizontal cross-sections show spin flow lines in the corresponding plane. Note that the spin is along e_z in the mid-plane and along e_ϕ away from it, and that it rotates in opposite direction above and below the mid-plane. See also the interactive version at <http://www.iap.fr/users/pichon/AM-near-saddle.html>.

For scale-invariant density power spectra with index n ($n - 4$ for the *potential*), s can be computed explicitly. At small separation, the term proportional to $\hat{r}^T \cdot \mathbf{H} \cdot \hat{r}$ goes like r^4 and is thus negligible compare to the rest (that scales like r^2). The spin coordinates in the frame of the Hessian are therefore quadrupolar

$$s \propto (f(\lambda_i, v, n)yz, g(\lambda_i, v, n)xz, h(\lambda_i, v, n)xy). \quad (27)$$

Fig. 12 illustrates the mean spin geometry around a typical saddle point. All the symmetry properties (anti-symmetry, octopole, ...) described in this section are clearly seen on this figure. In the plane of the saddle point, spins are aligned with the filament direction. When moving towards the nodes, the spins become more and more perpendicular (and more and more along e_ϕ).

4.1.3 Cosmic variance on 3D spin

It is of interest to also study the variance of the spin alignment $\sigma(\mathbf{r}|\text{ext}, I_1, \kappa_1, \kappa_2, v)$ defined as

$$\sigma = \sqrt{\langle \cos^2 \theta \rangle - \langle \cos \theta \rangle^2}, \quad (28)$$

where $\cos \theta = \mathbf{s} \cdot \mathbf{e}_z / \|\mathbf{s}\|$. It requires the numerical evaluation of a 12D integral. In contrast, the mean of the spin s (as computed in Section 4.1.2) or its square s^2 can be analytically computed.

We therefore propose to approximate the dispersion of the spin alignment with the following related estimator

$$\tilde{\sigma} = \sqrt{\frac{\langle s_z^2 \rangle - \langle s_z \rangle^2}{\langle \mathbf{s} \cdot \mathbf{s} \rangle}}, \quad (29)$$

where s_z is the component of the spin along the z -axis, i.e. along the filament direction. For the sake of readability, we do not write down the result of the integration here but display in Fig. 13 the map of the alignment dispersion $\tilde{\sigma}$ around a typical saddle point. This standard deviation is roughly constant around ≈ 0.6 and decreases to ≈ 0.3 in the close vicinity of the saddle point. Note that the spin direction is again best defined along its minor axis. This would be the best place to measure spin alignments in observations.

4.2 Mean saddle-point geometry

Here, we want to compute the mean values of $v, \lambda_1 < \lambda_2 < 0 < \lambda_3$ of a typical saddle point of filament type. Let us start from the so-called Doroshkevich formula for the PDF of these variables:

$$\mathcal{P}(v, \lambda_i) = \frac{135(5/2\pi)^{3/2}}{4\sqrt{1-\gamma^2}} \exp\left[-\frac{1}{2}\zeta^2 - 3I_1^2 + \frac{15}{2}I_2\right] \\ \times (\lambda_3 - \lambda_1)(\lambda_3 - \lambda_2)(\lambda_2 - \lambda_1),$$

where $\zeta = (v + \gamma I_1)/\sqrt{1-\gamma^2}$, $I_1 = \lambda_1 + \lambda_2 + \lambda_3$, $I_2 = \lambda_1\lambda_2 + \lambda_2\lambda_3 + \lambda_1\lambda_3$ and $I_3 = \lambda_1\lambda_2\lambda_3$. Subject to a saddle-point constraint, this PDF becomes

$$\mathcal{P}(v, \lambda_i|\text{sad}) = \frac{540\sqrt{5}\pi\mathcal{P}(v, \lambda_i)}{29\sqrt{2} + 12\sqrt{3}} I_3 \Theta(\lambda_3) \Theta(-\lambda_2), \quad (30)$$

after imposing the condition of saddle point $|\det \partial_i \partial_j \delta|\delta_D(\nabla\delta)\Theta(\lambda_3)\Theta(-\lambda_2)|$ for which as the gradient is decoupled from the density and the Hessian, only the condition on the sign of the eigenvalues and the determinant contribute. From this PDF, it is straightforward to compute the expected value of the density and the eigenvalues at a saddle-point position: $\langle v \rangle \approx 0.76\gamma$, $\langle \lambda_1 \rangle \approx -0.87$, $\langle \lambda_2 \rangle \approx -0.40$ and $\langle \lambda_3 \rangle \approx 0.51$. However, this saddle point does not belong to the skeleton of the density field but to its inter-skeleton (see Pogosyan et al. 2009). We thus want to impose an additional constraint which is $\lambda_2 + \lambda_3 < 0$. Let us call those saddle points ‘skeleton saddles’. The PDF at those points becomes

$$\mathcal{P}(v, \lambda_i|\text{skl}) = \frac{26460\sqrt{5}\pi\mathcal{P}(v, \lambda_i)I_3\Theta(\lambda_3)}{1421\sqrt{2} - 735\sqrt{3} + 66\sqrt{42}} \Theta(-\lambda_2 - \lambda_3). \quad (31)$$

The expected value of the density and the eigenvalues at a skeleton saddle position now becomes $\langle v \rangle \approx 1.25\gamma$, $\langle \lambda_1 \rangle \approx -1.0$, $\langle \lambda_2 \rangle \approx -0.56$ and $\langle \lambda_3 \rangle \approx 0.31$.

4.3 Spin flip: from spatial to mass transition

The geometry of the spin distribution near a typical skeleton saddle point (as defined by equation (31)) allows us to compute the mean alignment angle between the spin and the filament (see Section 4.3.1 below). In turn, the shape of the density profile in the vicinity of the same critical point, together with an extension of the Press-Schechter theory involving a filament-background split, allows us to estimate the ‘typical’ mass of the DM haloes forming in any spatial position around the saddle point (Section 4.3.2 below). The alignment-angle map and the typical-mass map will together yield a prediction for the transition mass.

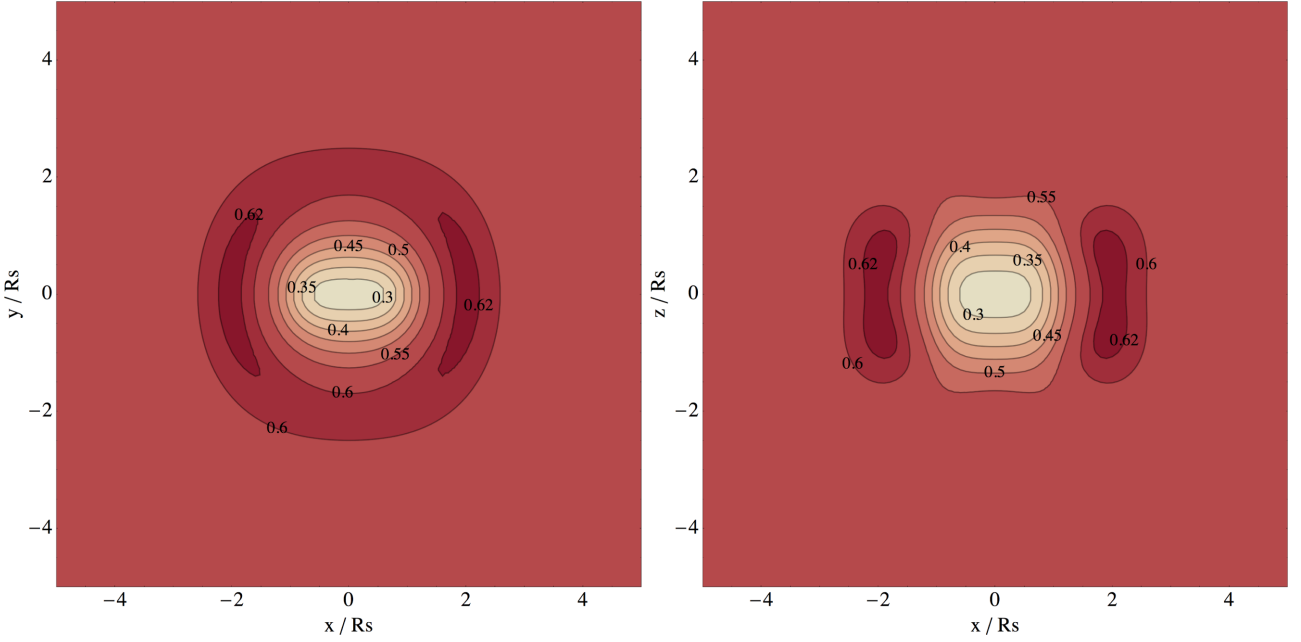


Figure 13. Alignment dispersion $\hat{\sigma}$ (defined in equation 29) around a typical filament-type saddle point of height $\nu = 1.25\gamma$, $\lambda_1 = 0.31$, $\lambda_2 = -0.56$, $\lambda_3 = -1$ for a power-law 3D power spectrum with spectral index $n = -2$. The left-hand panel displays a cut along the plane, Oxy , of the saddle point and right-hand panel along the plane, Oxz , of the wall. The uncertainty on spin direction is smallest near the saddle.

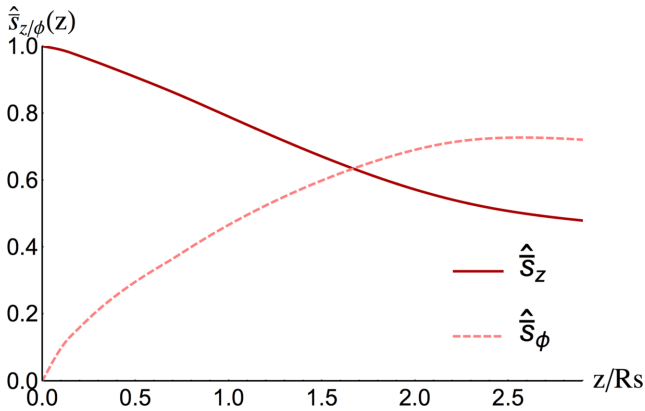


Figure 14. measure the height z corresponding to the transition from aligned to perpendicular to the filaments. The amplitude in both direction is averaged by plane following equation (32). The transition curvilinear coordinate is $z_{tr} = 1.5R_s$.

4.3.1 Spin flip along filaments

Section 4.1 showed that the mean spin flips from alignment in the plane of the saddle point to orthogonality when going towards the nodes. This can be quantified by measuring the curvilinear coordinate along the filament at which the spin flips.

Let us consider the mean *modulus* of the projection of the spin along the e_z - and e_ϕ -axes within a plane of height z

$$\hat{s}_{z/\phi}(z) = \int dx dy |\hat{s}_{z/\phi}(\mathbf{r})| / ||\mathbf{s}(\mathbf{r})||. \quad (32)$$

Fig. 14 displays $\hat{s}_{z/\phi}(z)$ as a function of z along the filament. Let us define $\hat{\theta}$ the flip angle so that

$$\cos \hat{\theta}(z) = \frac{\hat{s}_z(z)}{\sqrt{\hat{s}_z(z)^2 + \hat{s}_\phi(z)^2}} = \frac{1}{\sqrt{2}}. \quad (33)$$

In Fig. 14, this flip angle is found to occurs around $z = 1.5R_s$ which is very close to the r_* measured in two dimensions (see Section 3.2).

Alternatively, one can also compute at each position the mean alignment with the filament direction e_z

$$\cos \theta(\mathbf{r}) = \frac{\mathbf{s}(\mathbf{r}|\text{crit}) \cdot \mathbf{e}_z}{||\mathbf{s}(\mathbf{r}|\text{crit})||}. \quad (34)$$

The result is shown on the right-hand panel of Fig. 15. Spins tend to align with the filament (region in red) in the plane of the saddle point and becomes perpendicular to it when moving towards the nodes (region in blue). This is a transition in Lagrangian space. Section 4.3.2 shows how to convert it into a transition in mass.

4.3.2 Halo mass gradient along filament

The local mass distribution of haloes is expected to vary along the large-scale filament due to changes in the underlying long-wave density. In the linear regime, the typical overdensity near the end points (nodes) of the filament, where it joins the protocluster regions, may exceed the typical overdensity near the saddle point by a factor of 2 (Pogosyan et al. 1998). During epochs before the whole filamentary structure has collapsed, this leads to a shift in the hierarchy of the forming haloes towards larger masses near the filament end points (the clusters) relative to the filament middle point (the saddle). This can be easily understood using the formalism of barrier crossing (Peacock & Heavens 1990; Bond et al. 1991; Paranjape, Lam & Sheth 2012; Musso & Sheth 2012), which associates the density of objects of a given mass to the statistics for the random walk of halo density as the field is smoothed with decreasing filter sizes. Specifically, these authors predict the first upcrossing probability for the critical threshold at the filter scale corresponding to the mass of interest. The precise outcome of the formalism depends on the spectral properties of the field and the form of the smoothing filter, however it is clear that, in general, decreasing the barrier threshold increases the probability that such first upcrossing

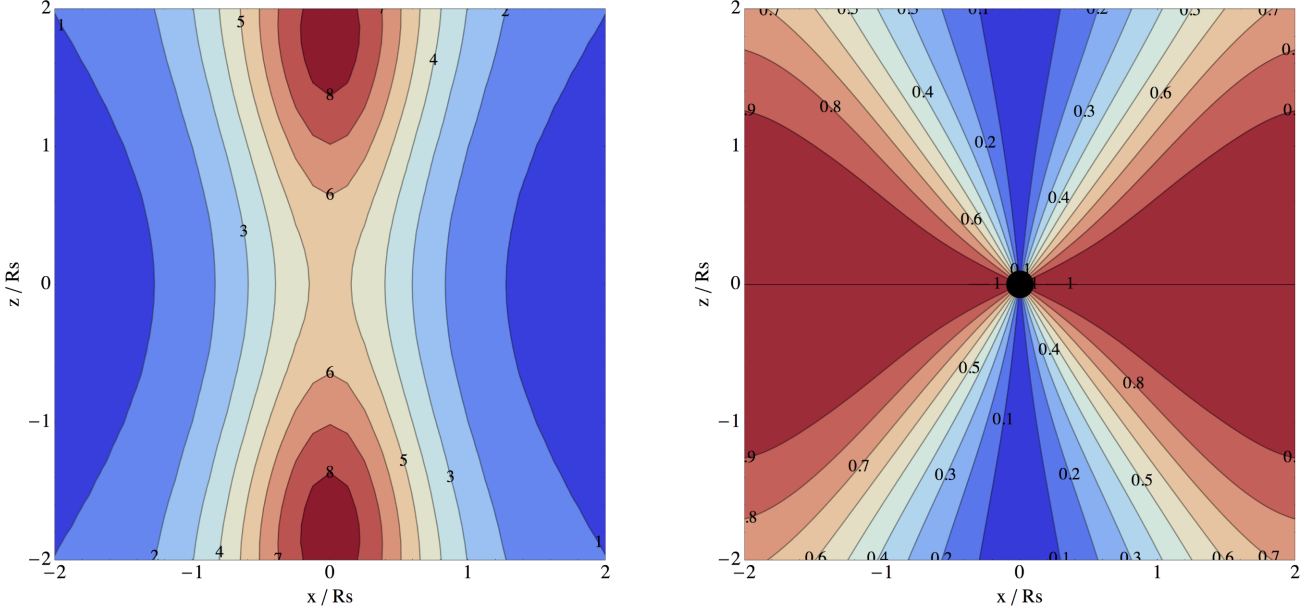


Figure 15. Left: cross-section of $M_p(r, z)$ (in units of $10^{12} M_\odot$) along the most likely filament and in the direction $x = y$. Right: corresponding cross-section of $(\cos \hat{\theta})(r, z)$, the normalized component of the spin aligned with the filament. The black dot represents the position of the saddle point. The mass of haloes increases towards the nodes, while the spin flips.

will happen at large smoothings, i.e. large mass. A larger fraction of the Lagrangian space will then belong to large-mass haloes, at the expense of the low-mass ones.

Following the presentation of Paranjape et al. (2012) of the Peacock–Heavens (Peacock & Heavens 1990) approximation – that was found to fit numerical simulations rather well, the number density of dark haloes in the interval $[M, M + dM]$ is

$$\frac{dn(M)}{dM} dM = \frac{\rho}{M} f(\sigma^2, \delta_c) d \ln \sigma^2, \quad (35)$$

where $f(\sigma^2, \delta_c)$ is given by the function

$$f(\sigma^2, \delta_c) = \exp \left(\frac{1}{\Gamma} \int_0^{\sigma^2} \frac{ds'}{s'} \ln p(s', \delta_c) \right) \times \left(-\sigma^2 \frac{dp(\sigma^2, \delta_c)}{d\sigma^2} - \frac{1}{\Gamma} p(\sigma^2, \delta_c) \ln p(\sigma^2, \delta_c) \right). \quad (36)$$

Here, σ^2 is the variance of the density fluctuations smoothed at the scale corresponding to M and $p(\sigma^2, \delta_c) \equiv 1/2(1 + \text{erf}(\delta_c/\sqrt{2}\sigma))$ is the probability of a Gaussian process with variance σ^2 to yield value below some critical threshold δ_c . In equation (36), Γ is the parameter dependent on the filtering scale and, to less extend the underlying power spectrum, that specifies how correlated the density values at the same point when smoothed at different scales are. For Gaussian filter, the value $\Gamma \approx 4$ is advocated.

The overall mass distribution of haloes is well described by the choice $\delta_c = 3/5(3\pi/2)^{2/3} = 1.681$, motivated by the so-called spherical collapse model. When haloes form on top of a large-scale structure background, however, the long-wave overdensity $\bar{\delta}(z)$ adds to the overdensity in the protohalo peaks. The effect on halo mass distribution, in this so-called peak-background-split approach, can be approximated as a *shifted* threshold $\delta_c(z) = 1.681 - \bar{\delta}(z)$ for halo formation. In Fig. 16, we show that, as expected, the result of this long-wavelength mode is a shift of the halo mass distribution towards larger masses. This shift can be characterized by the de-

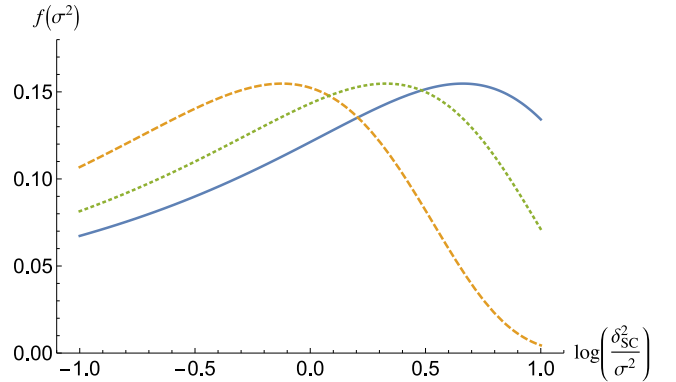


Figure 16. Mass distribution for three values of density threshold, $\delta_c = 1.681, 1, 0.681$ from left (yellow dashed line) to right (blue solid line). The displayed function $f(\sigma^2)$ is defined in equation (36).

pendence on the threshold of $M_*(\delta_c)$, defined as $\sigma_*(M_*) = \delta_c$, or of the mass $M_p(\delta_c)$ that corresponds to the peak of $f(\sigma^2, \delta_c)$, i.e. the variance $\sigma_p^2(z)$ defined by

$$\sigma_p^2(z) \equiv \underset{\sigma^2}{\text{argmax}}(f(\sigma^2, \delta_c(z))). \quad (37)$$

Fig. 17, right-hand axis, shows these two characteristic variances as functions of the threshold, δ_c .

The link to cosmology is established by relating the variance σ^2 to the mass of the objects. If a background field is absent, the variance is just the integral of the power spectrum $P(k)$ smoothed over a sphere of mass M

$$\sigma^2 = \sigma^2(M, Z) \equiv D^2(Z) \int k^2 dk P(k) W_{\text{TH}}^2((3M/4\pi\bar{\rho})^{1/3}),$$

where $D(Z)$ is the linear growing mode of perturbations as a function of redshift Z and W_{TH} is the top-hat filter. However, when large-scale structures are considered as fixed background, the variance of the

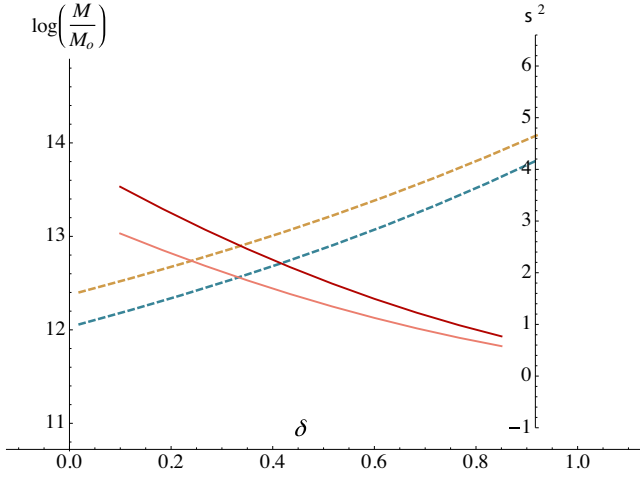


Figure 17. Characteristic variances (plain) and M_* (yellow dashed) and M_p halo masses (blue dashed) as functions of the large-scale density in the peak-background-split picture.

relevant small-scale density fluctuations that are responsible for object formation is reduced, approximately as

$$\sigma^2 \approx \sigma^2(M) - \sigma^2(M_{\text{LSS}}), \quad (38)$$

where $\sigma^2(M_{\text{LSS}})$, given as well as $\sigma^2(M)$ by equation (38), is the unconstrained variance at the scales at which we have defined the background large-scale density. This correction is negligible when there is distinct scale separation between non-linear forming objects and the large-scale density, i.e. $\delta(x) \ll 1.681$ but becomes important, truncating the mass hierarchy at M_{LSS} , whenever large-scale structures are themselves non-linear.

On Fig. 17, left-hand axis, the variances are converted into masses, M_* and M_p according to equation (38). We choose here $\sigma_8 = 0.8$, $Z = 0$, we define the mass in a $8h^{-1}$ Mpc comoving sphere for the best-fitting cosmological mass density and we approximate the spectrum with a power law of index $n = -2$, which allows to solve equation (38) explicitly, giving the $M(\sigma)$ relation as

$$M(\sigma, Z) = 2.6 \times 10^{14} M_{\odot} \left(\frac{\sigma^2 + \sigma^2(M_{\text{LSS}})}{\sigma_8^2 D(Z)^2} \right)^{-\frac{3}{n+3}}. \quad (39)$$

We consider filaments to be defined with $R = 5h^{-1}$ Mpc Gaussian smoothing, which gives $\sigma^2(M_{\text{LSS}}) \approx 0.66$. The evolution of $M_p(\delta, Z)$ follows from putting equation (37) into equation (39).

4.3.3 Spin orientation versus mass

From the above described M_p - δ relation, one can attribute a mass to each position depending on the value of the mean density at that location. The result is illustrated in Fig. 15 where the left- and right-hand panels display, respectively, the mass map and the spin alignment map around a typical saddle point. Eliminating the spatial position, \mathbf{r} , between these two maps yields $\langle \cos \theta \rangle$ as a function of M_p as shown on Fig. 18. The transition mass, \mathcal{M}_{tr} for spin flip ($\langle \cos \theta \rangle = 0.5$) is found to be of the order of $4 \times 10^{12} M_{\odot}$, assuming a smoothing scale of $5 \text{ Mpc } h^{-1}$, as used in Codis et al. (2012). This mass is in qualitative agreement with the transition mass found in that paper, all the more so as the redshift evolution of this transition mass will also be consistent (scaling as the mass of non-linearity).

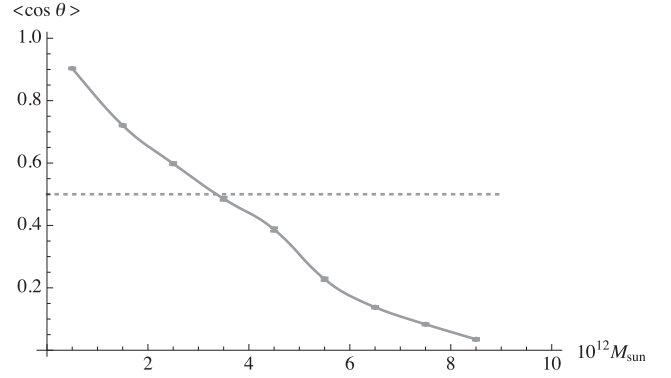


Figure 18. Mean alignment as a function of mass for a smoothing scale for filaments of $5 \text{ Mpc } h^{-1}$. Error bars represent the error on the mean cosine in each bin of mass for the region $[-2R_s, 2R_s] \times [-2R_s, 2R_s] \times [-2R_s, 2R_s]$ around a typical filament-saddle point. The flip transition mass corresponds to $4 \times 10^{12} M_{\odot}$.

It is quite striking that the geometry of the saddle point alone allows us to predict this mass. The two main ingredients for success are the point reflection symmetry of the spin distribution near the most likely filament-like saddle point on the one hand, and the peak-background-split mass distribution gradient along the filament towards the nodes of the cosmic web on the other hand.

5 STATISTICS

Up to now, we have considered the neighbourhood of a *given unique* typical saddle point as a proxy for the behaviour within a GRF. In view of our finding let us now first analyse the statistics of alignment for GRF, and then for fields corresponding to their simulated cosmic evolution down to redshift zero.

5.1 Validation on GRF

Let us consider the following experiment. Let us generate 2D or 3D realizations of GRF smoothed on two successive scales, L_h and $L_s \gg L_h$. In the first maps, let us build a catalogue of positions, \mathbf{r}_h and heights, v_h corresponding to ‘small-scale’ peaks. From the second maps, let us identify the loci, \mathbf{r}_s of the corresponding ‘large-scale’ peaks (in 2D) and (filament-type) saddles (in 3D), and build the corresponding fields $s(\mathbf{r})$ (via `fft` using equation 24). This field allows us to assign a spin to each ‘halo’ at position \mathbf{r}_h and a closest saddle, \mathbf{r}_s . Given the relative position $\mathbf{r}_h - \mathbf{r}_s$ as measured in the frame defined by the Hessian at \mathbf{r}_s , we may project the direction of the spins, $\hat{s} \equiv s/s$ of all ‘haloes’ in the vicinity along the corresponding local cylindrical coordinate $(\mathbf{e}_R, \mathbf{e}_\phi, \mathbf{e}_z)$. We may then compute the one-point statistics of $\mu_z \equiv \hat{s} \cdot \mathbf{e}_z$ per octant.

5.1.1 2D GRF fields spin flip

In two dimensions, the expectation is that the spin should be aligned or anti-aligned with \mathbf{e}_z depending on each quadrant.

Let us first start with a set of 25 2D 2048^2 maps from a power spectrum with $n = -1/2$. The map is first smoothed with Gaussian filter of width $L_h = 4$ pixels, and the positions of the peaks are identified. It is then smoothed again over $L_s = 24$ pixels, exponentiated (in order to mimic the almost lognormal statistics of the evolved cosmic density field), and the corresponding Hessian and tidal fields are computed, together with the momentum map, which

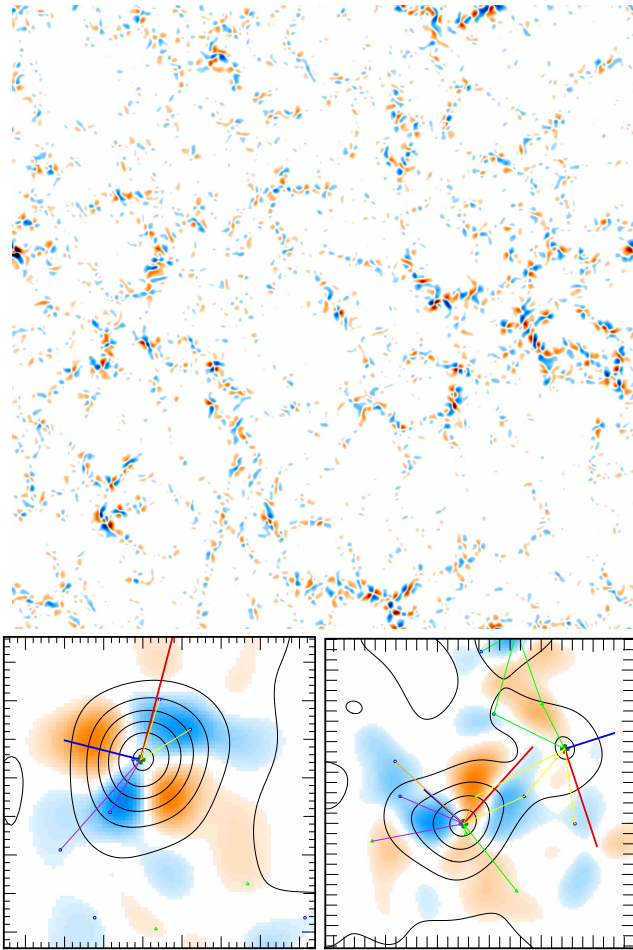


Figure 19. Top: example of spin map (colour coded by sign) generated following the prescription of Section 5.1.1. Bottom: the local frame (in red, long axis and blue) around a couple of ‘saddle’s. The black contours correspond to the density.

is thresholded above 1/30th of its highest value (see Fig. 19). The peaks of this second map are identified as ‘saddles’ for contrasts higher than 2.5. Fig. 20 shows that the average spin of ‘haloes’ in each quadrant is flipping from one quadrant to the next, with a statistically significant non-zero mean value in each quadrant.

5.1.2 3D GRF fields spin flip

Let us similarly consider a set of 20 three-dimensional 256^3 cubes from a power spectrum with $n = -2$. The cube is first smoothed with Gaussian filter of width $L_h = 4$ pixels, and the positions of the peaks are identified. It is then smoothed again over $L_s = 24$ pixels, exponentiated, and the corresponding Hessian and tidal fields are computed, together with the spin field, which is thresholded above 1/30th of its highest value. The saddle of this second cube are identified as for contrasts higher than 1. Only peaks closer than one smoothing length from the large-scale saddles are kept. The angle between their spin and the filament axis is computed and stored depending on the octant they belong to. In this section, the octants are numbered from 1 to 8 depending on the separation from the peak to the saddle $\mathbf{r} = (x, y, z)$: $x, y, z > 0$ (#1), $x < 0$ and $y, z > 0$ (#2), $x, y < 0$ and $z > 0$ (#3), $y < 0$ and $x, z > 0$ (#4), $z < 0$ and $x, y > 0$ (#5), $x, z < 0$ and $y > 0$ (#6), $x, y, z < 0$ (#7), and $y, z < 0$ and $x > 0$ (#8).

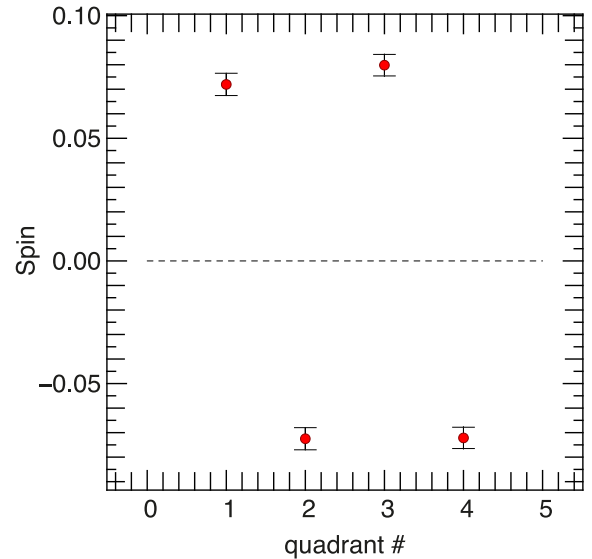


Figure 20. Alignment of ‘spin’ along \mathbf{e}_z in two dimensions as a function of quadrant rank, clockwise. As expected, from one quadrant to the next, the spin is on average unambiguously flipping sign.

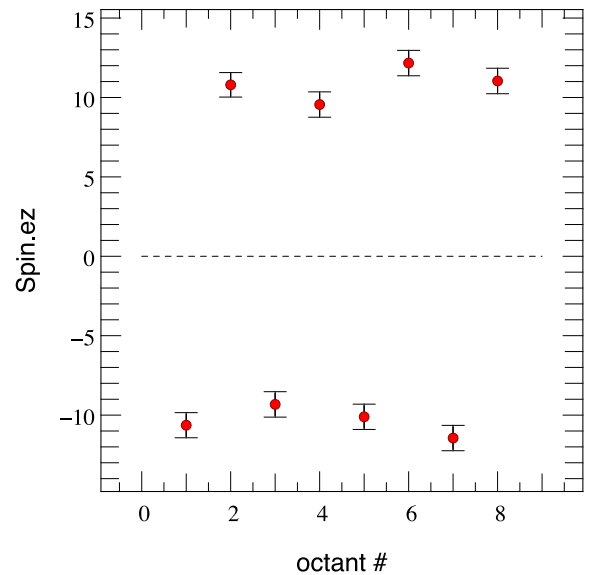


Figure 21. Alignment of the spin along the filamentary direction depending on the considered octant. As predicted by the theory, the z -component of the spin is flipping sign from one octant to the other.

(#8). Fig. 21 shows that, as expected, the component of the spin aligned with the filament axis is flipping sign from one octant to the other.

5.2 Validation on dark matter simulations at $z = 0$

Let us now identify the Eulerian implication at redshift zero of the above sketched Lagrangian theory. For this, we must rely on N -body simulations. Hence, we now make use of the 43 million DM haloes detected at redshift zero in the Horizon-4 π N -body simulation (Teyssier et al. 2009) to test some of the outcomes of the anisotropic tidal torque theory presented in this paper. This simulation contains 4096^3 DM particles distributed in a $2 h^{-1}$ Gpc periodic box and is characterized by the following Λ CDM cosmology:

$\Omega_m = 0.24$, $\Omega_\Lambda = 0.76$, $n = 0.958$, $H_0 = 73 \text{ km s}^{-1} \text{ Mpc}^{-1}$ and $\sigma_8 = 0.77$ within one standard deviation of WMAP3 results (Spergel et al. 2003). The initial conditions were evolved non-linearly down to redshift zero using the adaptive mesh refinement code RAMSES (Teyssier 2002), on a 4096^3 grid. The motion of the particles was followed with a multigrid Particle-Mesh Poisson solver using a cloud-in-cell interpolation algorithm to assign these particles to the grid (the refinement strategy of 40 particles as a threshold for refinement allowed us to reach a constant physical resolution of 10 kpc, see the above-mentioned two references).

The Friend-of-Friend Algorithm (Huchra & Geller 1982) was used over 18^3 overlapping subsets of the simulation with a linking length of 0.2 times the mean inter-particle distance to define DM haloes. In the present work, we only consider haloes with more than 40 particles (the particle mass being $7.7 \times 10^9 M_\odot$). The mass dynamical range of this simulation spans about five decades.

The filament's direction is then defined via the global skeleton algorithm introduced by Sousbie, Colombi & Pichon (2009) and based on Morse theory. It defines the skeleton as the set of critical lines joining the maxima of the density field through saddle points following the gradient. In practice, Sousbie et al. (2009) define the peak and void patches of the density field as the set of points converging to a specific local maximum/minimum while following the field lines in the direction/opposite direction of the gradient. The skeleton is then the set of intersection of the void patches, i.e. the subset of critical lines connecting the saddle points and the local maxima of a density field and parallel to the gradient of the field. In practice, the ~ 70 billion particles of the Horizon-4 π were sampled on a 2048^3 Cartesian grid and the density field was smoothed using `mpsmooth` (Prunet et al. 2008) over a scale of $5 h^{-1} \text{ Mpc}$ corresponding to a mass of $1.9 \times 10^{14} M_\odot$. This cube was then divided into 6^3 overlapping subcubes and the skeleton was computed for each of these subcubes. It was then reconnected across the entire simulation volume to produce a catalogue of segments which locally defines the direction of the filaments.

Fig. 22 demonstrates that the spins of the 43 million dark haloes of the simulation obey the expected mass-dependent flip predicted by the theory presented in Section 4. On top of the alignment with the filament direction found, e.g. in Codis et al. (2012), haloes are shown to have a spin increasingly perpendicular to e_ϕ at low-mass (red) and up to the critical mass ($\simeq 10^{12} M_\odot$), while high-mass haloes have a spin parallel to the e_ϕ direction. The transition from alignment to orthogonality occurs around $M_{\text{tr}} \simeq 5 \times 10^{12} M_\odot$.

Fig. 23 shows that the spins tend to be more aligned with the filament axis when getting closer to the saddle point. The alignment decreases from $\cos \theta = 0.511$ at $r \simeq 20 \text{ Mpc } h^{-1}$ to $\cos \theta = 0.506$ at $r < 1 \text{ Mpc } h^{-1}$. This qualitative trend is in full agreement with the anisotropic tidal torque theory picture presented in Section 4 for which on average, spins are aligned with the filament axis in the plane of the saddle point and become misaligned when going away from this saddle point.

Fig. 24 displays the occupancy of haloes along the filaments. It appears that the higher the mass, the more concentrated they are far from the saddles. This is in good agreement with the halo mass gradient along the filaments described in Section 4.3.2.

Overall, the above GRF experiments as well as the re-analysis of the Horizon-4 π N -body simulation seem consistent with the prediction of the theory presented in Sections 3 and 4. While the former demonstrates that interferences from neighbouring saddles do not wash out the tide correlations, the latter suggests that on the scales probed by this experiment, this Eulerian measure still captures features of the underlying Lagrangian theory.

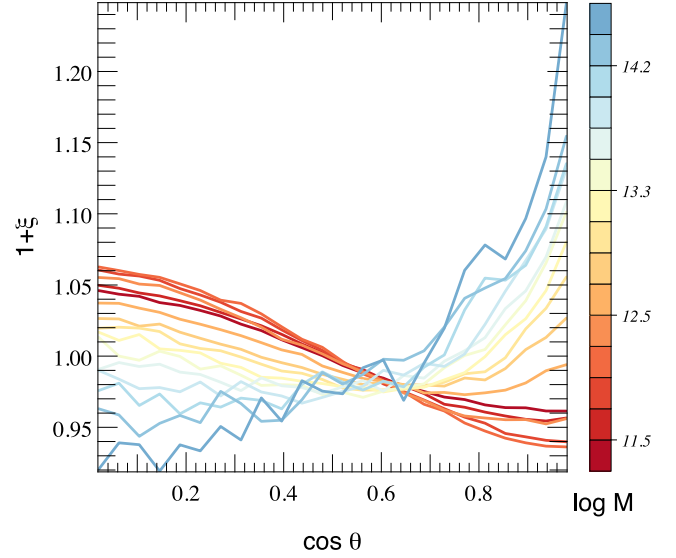


Figure 22. Alignment of ‘spin’ along e_ϕ in the Horizon-4 π simulation. The normalized histogram of the cosine of the angle between the spins and the closest filament’s direction is displayed. Deviations from the $\xi = 0$ uniform distribution are detected and depends on the dark matter halo mass. Haloes have a spin aligned with the e_ϕ direction on average at low-mass (red) and perpendicular to it at larger mass (blue).

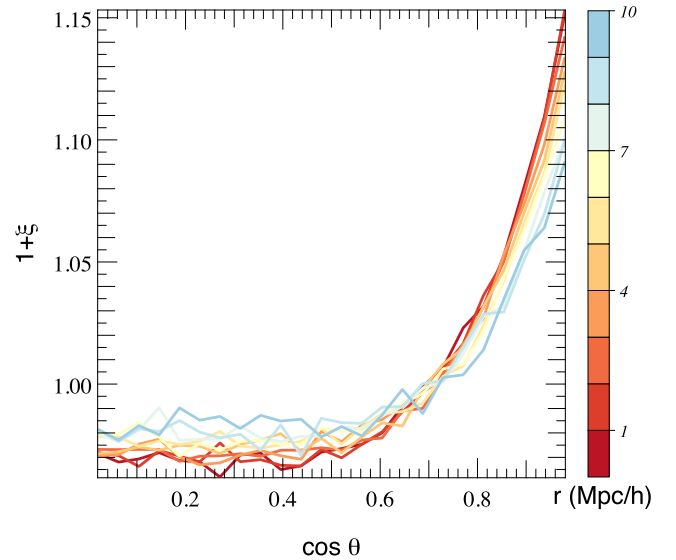


Figure 23. Alignment of the spins and the filaments in the Horizon-4 π simulation as a function of the distance to the closest saddle point (from red – 0 – to blue – 10 $\text{Mpc } h^{-1}$). The alignment decreases with the distance to the saddle point as predicted by the anisotropic tidal torque theory model.

6 CONCLUSIONS AND PERSPECTIVES

TTT was revisited while focusing on an anisotropic peak-background-split in the vicinity of a saddle point. Such critical point captures as a point process the geometry of a typical filament embedded in a given wall (Pogosyan et al. 1998). The induced misalignment between the tidal tensor and the Hessian of the density simply explains the surrounding transverse and longitudinal point reflection-symmetric geometry of the spin distribution near filaments. This geometry of the spin field predicts in particular that less massive galaxies have their spin parallel to the filament, while more massive ones have their spin in the azimuthal direction. The

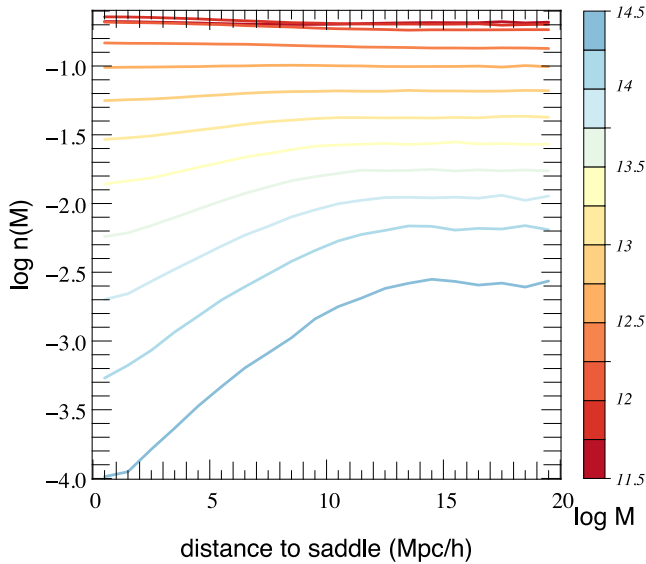


Figure 24. (log-)fraction of haloes of different mass (from red to blue in solar mass units) as a function of the distance to the saddle point in the Horizon-4 π simulation. Low-mass haloes (red) lie almost uniformly along the filaments (with a small concentration – not clearly seen in logarithmic units – around the saddles due to consumption when going towards the nodes) while high-mass haloes (blue) are more concentrated far from the saddles.

corresponding transition mass follows from this geometry together with its scaling with the mass of non-linearity, in good agreement with measurements in simulations.

The main findings of this paper are: (i) galaxies form near filaments embedded in walls, and flow towards the nodes: this anisotropic environment produces the long wave modes on top of which galactic haloes pass the turnaround threshold; (ii) a typical filament is elongated and flattened: as a point process, it is therefore best characterized by its triaxial saddle points; (iii) the spin geometry is octupolar in the vicinity of the saddle point, displaying a point reflection symmetry; (iv) the mean spin field is parallel to the filament axis in the plane of the saddle point and becomes azimuthal away from it; (v) the constrained tidal torque theory presented in this paper allows to accurately predict the transition mass of the spin-filament alignment measured in simulations; (vi) this theory seems consistent with both GRF experiments and results from N -body simulations; (vii) a dual theory describes spin alignments in voids (see Appendix B).

6.1 Discussion

One of the striking features of this anisotropic extension of TTT is the induced quadrupolar point-symmetric flattened geometry of the spin distribution near a saddle point, which effectively scales down by 1 order of magnitude the transition mass away from the mass of non-linearity, in agreement with the measured scaling. The qualitative analysis derived from first principles in the vicinity of a given saddle point seems to hold when considering realizations of GRF, once proper account of the induced geometry near such points is taken care of. In effect, we have shown that the geometry of the saddle point provides a natural ‘metric’ (the local frame as defined by the Hessian at that saddle point) relative to which we can study the dynamical evolution of dark haloes along filaments. It should allow us to study how galactic feeding (via helicoidal cold flow; see

Dubois et al. 2014) should vary with curvilinear coordinate along the filament. It was indeed found in that paper using hydrodynamical simulations that such flows were reaching galaxies in the so-called circum-galactic medium with velocities roughly parallel the polar axis. Taken at face value, such findings suggest that the flow feeding galaxies has significant helicity during that phase.

Another striking feature of this *Lagrangian* framework is that it captures naturally the arguably non-linear *Eulerian* process of spin flip via mergers. Recently, Laigle et al. (2015) showed that angular momentum generation of haloes could be captured in Eulerian space via the secondary advection of vorticity which the formation of the filament generates, whereas we show in this paper that it may also be described in Lagrangian space via the analysis of the anisotropic tides generated by the filament to be. No description is more fundamental than the other but are the two (Eulerian versus Lagrangian) sides of the same coin. The mapping between the two descriptions requires a reversible time integrator, such as the Zel’dovich approximation, which clearly limits its temporal validity to weakly non-linear scales. Our proxy for the spin, equation (3), is an approximation which seems to quantitatively capture the relevant physics. It is remarkable that such an (admittedly approximate) straightforward extension of TTT captures what seems to be the driving process of spin orientation acquisition and its initial evolution. It is also striking that very simple closed form for the spin orientation distribution in the vicinity of the saddle point are available for this proxy.

Our theory here has focused on a two-scale process. Given the characteristics of Λ CDM hierarchical clustering, one can anticipate that this process occurs on several nested scales at various epochs – and arguably on various scales at the same epoch. The scenario we propose for the origin of this signal is, like the signal itself, relative to the linear scale involved in defining the filaments and as such, multiscale. It will hold as long as filaments are well defined in order to drive the local cosmic flow. In other words, one expects smaller scale filaments are themselves embedded in larger scale walls. The induced multiscale anisotropic flow transpires in the scaling of the transition mass with smoothing, as discussed in Codis et al. (2012).

Of course, we have here completely ignored the effect of feedback, which will play some – yet undefined – role in redistributing the cosmic pristine gas falling on to forming galaxies. Another issue would be to estimate for how long this entanglement between the large-scale dynamics and the kinematic properties of high redshift pervades, given the disruptions induced by feedback. What will be the effect of AGN feedback (Dubois et al. 2013; Prieto et al. 2015) on tidally biased secondary infall? Ocvirk, Pichon & Teyssier (2008) have also shown that at lower redshift, the so-called hot mode of accretion will kick in; how will hot flows wash out/disintegrate these ribbons? Given that they locally reflect the large-scale geometry, will the gas continue to flow-in along preferred directions (as does the DM; see e.g. Aubert, Pichon & Colombi 2004), or does the hot phase erase any anisotropy? Will the above-mentioned smaller scale non-linear dynamics eventually wash out any such trace?

6.2 Perspectives

One possibly significant shortcoming of the analysis is the proxy involved in using the Hessian of the density instead of the inertia tensor (though see Appendix A1). This is critical in order to retain a point process for the induced spin, but is achieved at the expense of having an adequate estimate for the *amplitude* of the spin, which is unfortunate because from the point of view of morphology, the dividing line between spirals and ellipticals is likely to be spin

amplitude. Let us none the less assume that, e.g. match to simulations or ansatz such as those described in Schäfer & Merkel (2012) will yield access to reasonable fit to spin amplitude and discuss briefly implications to galaxy formation within its cosmic web.

6.2.1 Epoch of maximal spin advection?

The inspection of hydrodynamical simulations (e.g. Codis et al. 2012, using tracer particles) shows that ribbon-like caustics feed the central galaxy along its spin axis from both poles. The gas flowing roughly parallel to the spin axis of the disc along both directions will typically impact the disc's circum-galactic medium and shock once more (as it did when it first reached the wall, and then the filaments, forming those above-mentioned ribbons), radiating away its vertical momentum (see Tillson et al. 2015). These ribbons are generated via the same winding/folding process as the protogalaxy, and represent the dominant source of secondary filamentary infall which feeds the newly formed galaxy with gas of well-aligned angular momentum.

Having computed the most likely spin (direction) as a function of position, it is therefore of interest to measure its covariant polar flux through a drifting forming galaxy.

From our knowledge of the spin distribution within the neighbourhood of a given saddle, we may then compute the rate of advected spin within some galactic volume $\mathcal{V} = S\Delta z$; it reads

$$\begin{aligned} \dot{s} &= \int d^2S \cdot \mathbf{v} \otimes \rho s = \int_{\mathcal{V}} d^3\mathbf{r} \nabla \cdot (\rho \mathbf{v} \otimes s), \\ &\approx S [\rho \mathbf{v} \otimes s]_{-}^{+} \approx S\Delta z \frac{\partial}{\partial z} (\rho v_z s_z), \end{aligned} \quad (40)$$

where the last equality assumes that the advection is quasi-polar, and that the spin is mostly aligned with the filament. In equation (40), \mathbf{v} is the gradient of the potential. Let us identify the curvilinear coordinate, z_{up} , for which this flux is maximal:

$$z_{\text{up}} = \operatorname{argmax}_z \frac{\partial}{\partial z} (\rho v_z s_z) = \left\{ z \left| \frac{\partial^2}{\partial z^2} (\rho v_z s_z) = 0 \right. \right\}. \quad (41)$$

The coordinate $z_{\text{up}}(v, \kappa_1, \kappa_2)$ characterizes the most active regions in the cosmic web for galactic spin-up. Focusing on the most likely saddle, the argument sketched in Section 4.3.2 allows us to assign a redshift-dependent spin-up mass, $\mathcal{M}_{\text{up}}(Z)$, via equations (37) and (39). There could be an observational signature, e.g. in terms of the cosmic evolution of the SFR, as maximum spin-up corresponds to efficient pristine cold and dense gas accretion, which in turn induces consistent and steady star formation.

6.2.2 Morphological type versus loci on web?

The magnitude of the spin of galaxies could be taken as a proxy for morphological type. Indeed, Welker et al. (2014, 2015) have shown in cosmological hydrodynamical simulations that spin direction and galactic sizes where sensitive to the anisotropic environment. It is shown in particular that the magnitude of the spin of simulated galaxies increases steadily and aligns itself preferentially with the nearest filament when no significant merger occurs, in agreement with the first phase of the above described spin-up (see also Pichon et al. 2011). During that phase, the fraction of larger spirals should increase. In contrast, following Fig. 24, if we account for the fact that galactic morphology – the fraction of ellipticals, correlates with dark halo mass, it should then increase with distance to saddle.

In order to tackle such process theoretically, it would therefore be worthwhile to revisit Quinn & Binney (1992) in the context

of this constrained theory of tidal torques and quantify how the dynamics of concentric shells are differentially biased by the tides of a saddle point. This would allow us to describe the whole timeline of anisotropic secondary infall.

6.2.3 Implication for weak lensing?

Weak lensing attempts to probe the statistics of the cosmic web between background galaxies – which shape is assumed to be uncorrelated – and the observer, while assuming that observed shape statistics reflects the deflection of light going through the intervening web. In view of Fig. 12, if we take as a proxy spin alignment for shape alignment, we can in principle compute the expectation of $\xi(\Delta\mathbf{r}) \equiv \langle s(\mathbf{r}) \cdot s(\mathbf{r}') | \text{skl} \rangle$ as a function of $\Delta\mathbf{r} = \mathbf{r} - \mathbf{r}'$. Calling $\delta s = s - \langle s(\mathbf{r}) | \text{skl} \rangle$, we have $\xi(\Delta\mathbf{r}) = \langle s(\mathbf{r}) | \text{skl} \rangle \cdot \langle s(\mathbf{r}') | \text{skl} \rangle + \langle \delta s(\mathbf{r}) \cdot \delta s(\mathbf{r}') | \text{skl} \rangle + 2\langle \delta s(\mathbf{r}) \cdot s(\mathbf{r}') | \text{skl} \rangle$. Let us just focus here on the first term, $\langle s(\mathbf{r}) | \text{skl} \rangle \cdot \langle s(\mathbf{r}') | \text{skl} \rangle$. Given equation (25), we can compute it and find that it will typically be non-zero and vary significantly depending on both the magnitude and the orientation of $\Delta\mathbf{r}$. E.g. if $\Delta\mathbf{r}$ is off-axis along the filament, but if the pair is close to the saddle and $|\Delta\mathbf{r}|$ is small it will be positive (spins will align as they are both within coherent region of the saddle's tides), while if $|\Delta\mathbf{r}|$ is somewhat larger it will vanish (spins will be perpendicular). Conversely, if $\Delta\mathbf{r}$ is transverse to the filament and $|\Delta\mathbf{r}|$ is small, it will be positive, but if $|\Delta\mathbf{r}|$ is of the order of the size of one octant it will typically vanish again. The formalism presented in Section 3.1 can clearly be extended (while considering the joint three points statistics) to predict exactly all terms involved in $\xi(\Delta\mathbf{r})$ and quantify within this framework the effect of intrinsic alignments on the spin-spin two-point correlation. This is will be to topic of future work (Codis et al., in preparation).

ACKNOWLEDGEMENTS

This work is partially supported by the Spin(e) grants ANR-13-BS05-0005 (<http://cosmicorigin.org>) of the French *Agence Nationale de la Recherche* and by the ILP LABEX (under reference ANR-10-LABX-63 and ANR-11-IDEX-0004-02). CP thanks D. Lynden-bell for suggesting to tackle this problem and Churchill college for hospitality while this work was completed. Many thanks to J. Devriendt, A. Slyz, J. Binney, Y. Dubois, V. Desjacques, C. Laigle and S. Prunet for discussions about tidal torque theory, and to our collaborators of the Horizon project (<http://projet-horizon.fr>) for helping us produce the Horizon-4 π simulation, F. Bouchet for allowing us to use the MAGIQUE3 supercomputer during commissioning, and to S. Rouberol for making it possible, and running the horizon cluster for us. SC and CP thank Lena for her hospitality when this work was initiated, and Eric for his help with some figures.

REFERENCES

- Aragón-Calvo M. A., Yang L. F., 2014, MNRAS, 440, L46
 Aragón-Calvo M. A., van de Weygaert R., Jones B. J. T., van der Hulst J. M., 2007, ApJ, 655, L5
 Aubert D., Pichon C., Colombi S., 2004, MNRAS, 352, 376
 Bailin J., Steinmetz M., 2005, ApJ, 627, 647
 Bardeen J. M., Bond J. R., Kaiser N., Szalay A. S., 1986, ApJ, 304, 15
 Bernstein G. M., Norberg P., 2002, AJ, 124, 733
 Bond J. R., Cole S., Efstathiou G., Kaiser N., 1991, ApJ, 379, 440
 Bond J. R., Kofman L., Pogosyan D., 1996, Nature, 380, 603
 Brown M. L., Taylor A. N., Hambly N. C., Dye S., 2002, MNRAS, 333, 501

- Catelan P., Theuns T., 1996, *MNRAS*, 282, 436
 Catelan P., Kamionkowski M., Blandford R. D., 2001, *MNRAS*, 320, L7
 Codis S., Pichon C., Devriendt J., Slyz A., Pogosyan D., Dubois Y., Soubis T., 2012, *MNRAS*, 427, 3320
 Codis S. et al., 2015, *MNRAS*, 448, 3391
 Crittenden R. G., Natarajan P., Pen U.-L., Theuns T., 2001, *ApJ*, 559, 552
 Croft R. A. C., Metzler C. A., 2000, *ApJ*, 545, 561
 Danovich M., Dekel A., Hahn O., Teyssier R., 2012, *MNRAS*, 422, 1732
 Doroshkevich A. G., 1970, *Astrophysics*, 6, 320
 Dubois Y., Pichon C., Haehnelt M., Kimm T., Slyz A., Devriendt J., Pogosyan D., 2012, *MNRAS*, 423, 3616
 Dubois Y., Pichon C., Devriendt J., Silk J., Haehnelt M., Kimm T., Slyz A., 2013, *MNRAS*, 428, 2885
 Dubois Y. et al., 2014, *MNRAS*, 444, 1453
 Forero-Romero J. E., Contreras S., Padilla N., 2014, *MNRAS*, 443, 1090
 Gunn J. E., Gott J. R., III, 1972, *ApJ*, 176, 1
 Hahn O., Porciani C., Carollo C. M., Dekel A., 2007, *MNRAS*, 375, 489
 Heavens A., Refregier A., Heymans C., 2000, *MNRAS*, 319, 649
 Heymans C., Brown M., Heavens A., Meisenheimer K., Taylor A., Wolf C., 2004, *MNRAS*, 347, 895
 Hirata C. M., Seljak U., 2004, *Phys. Rev. D*, 70, 063526
 Hirata C. M. et al., 2004, *MNRAS*, 353, 529
 Hirata C. M., Mandelbaum R., Ishak M., Seljak U., Nichol R., Pimblet K. A., Ross N. P., Wake D., 2007, *MNRAS*, 381, 1197
 Hoyle F., 1949, *Problems of Cosmical Aerodynamics*. Central Air Documents, Office, Dayton, OH
 Huchra J. P., Geller M. J., 1982, *ApJ*, 257, 423
 Joachimi B., Mandelbaum R., Abdalla F. B., Bridle S. L., 2011, *A&A*, 527, A26
 Joachimi B., Semboloni E., Bett P. E., Hartlap J., Hilbert S., Hoekstra H., Schneider P., Schrabback T., 2013a, *MNRAS*, 431, 477
 Joachimi B., Semboloni E., Hilbert S., Bett P. E., Hartlap J., Hoekstra H., Schneider P., 2013b, *MNRAS*, 436, 819
 Klypin A., Shandarin S. F., 1993, *ApJ*, 413, 48
 Laigle C. et al., 2015, *MNRAS*, 446, 2744
 Lee J., Pen U., 2000, *ApJ*, 532, L5
 Lee J., Pen U.-L., 2002, *ApJ*, 567, L111
 Libeskind N. I., Hoffman Y., Forero-Romero J., Gottlöber S., Knebe A., Steinmetz M., Klypin A., 2013, *MNRAS*, 428, 2489
 Mandelbaum R., Hirata C. M., Ishak M., Seljak U., Brinkmann J., 2006, *MNRAS*, 367, 611
 Mandelbaum R. et al., 2011, *MNRAS*, 410, 844
 Musso M., Sheth R. K., 2012, *MNRAS*, 423, L102
 Ocvirk P., Pichon C., Teyssier R., 2008, *MNRAS*, 390, 1326
 Paranjape A., Lam T. Y., Sheth R. K., 2012, *MNRAS*, 420, 1429
 Paz D. J., Staszyszyn F., Padilla N. D., 2008, *MNRAS*, 389, 1127P
 Peacock J. A., Heavens A. F., 1990, *MNRAS*, 243, 133
 Peebles P. J. E., 1969, *ApJ*, 155, 393
 Pichon C., Bernardeau F., 1999, *A&A*, 343, 663
 Pichon C., Pogosyan D., Kimm T., Slyz A., Devriendt J., Dubois Y., 2011, *MNRAS*, pp 1739
 Pogosyan D., Bond J. R., Kofman L., Wadsley J., 1998, in *Colombi S., Mellier Y., Raban B., eds, Wide Field Surveys in Cosmology*, Editions Frontieres, Paris, p. 61
 Pogosyan D., Pichon C., Gay C., Prunet S., Cardoso J. F., Soubis T., Colombi S., 2009, *MNRAS*, 396, 635
 Porciani C., Dekel A., Hoffman Y., 2002, *MNRAS*, 332, 325
 Prieto J., Jimenez R., Haiman Z., González R. E., 2015, *MNRAS*, 452, 784
 Prunet S., Pichon C., Aubert D., Pogosyan D., Teyssier R., Gottlöber S., 2008, *ApJS*, 178, 179
 Quinn T., Binney J., 1992, *MNRAS*, 255, 729
 Schaefer B. M., 2009, *Int. J. Mod. Phys. D*, 18, 173
 Schäfer B. M., Merkel P. M., 2012, *MNRAS*, 421, 2751
 Schneider M. D., Bridle S., 2010, *MNRAS*, 402, 2127
 Schneider M. D., Frenk C. S., Cole S., 2012, *J. Cosmol. Astropart. Phys.*, 5, 30
 Soubis T., Pichon C., Colombi S., Pogosyan D., 2008, *MNRAS*, 383, 1655
 Soubis T., Colombi S., Pichon C., 2009, *MNRAS*, 393, 457
 Spergel D. N. et al., 2003, *ApJS*, 148, 175
 Stewart K. R., Brooks A. M., Bullock J. S., Maller A. H., Diemand J., Wadsley J., Moustakas L. A., 2013, *ApJ*, 769, 74
 Tempel E., Stoica R. S., Saar E., 2013, *MNRAS*, 428, 1827
 Tenneti A., Singh S., Mandelbaum R., Matteo T. D., Feng Y., Khandai N., 2015, *MNRAS*, 448, 3522
 Teyssier R., 2002, *A&A*, 385, 337
 Teyssier R. et al., 2009, *A&A*, 497, 335
 Tillson H., Devriendt J., Slyz A., Miller L., Pichon C., 2015, *MNRAS*, 449, 4363
 Welker C., Devriendt J., Dubois Y., Pichon C., Peirani S., 2014, *MNRAS*, 445, L46
 Welker C., Dubois Y., Devriendt J., Pichon C., 2015, preprint (arXiv:1510.4061)
 White S. D. M., 1984, *ApJ*, 286, 38
 White S. D. M., Tully R. B., Davis M., 1988, *ApJ*, 333, L45
 Zel'dovich Y. B., 1970, *A&A*, 5, 84
 Zhang Y., Yang X., Faltenbacher A., Springel V., Lin W., Wang H., 2009, *ApJ*, 706, 747

APPENDIX A: A MULTISCALE THEORY

The proxy we take for the spin direction

$$s_i = \sum_{j,k,l} \epsilon_{ijk} H_{jl} T_{lk}, \quad (\text{A1})$$

is, as mentioned in the main text, a (quadratic) approximation. First, because equation (1) is only valid in the linear regime (Porciani, Dekel & Hoffman 2002), but possibly more importantly because we take the Hessian as a proxy for the inertia tensor. In practice, recall that this approximation seems nevertheless to capture the essence of the processes at work in aligning spins with the large-scale structure given its ability to explain observed alignments through the comparison with simulations presented in Section 5.2 together with the measured mass transition. This suggests experimentally that it is indeed reasonable. Notwithstanding, while H_{ij} and I_{ij} locally share the same eigenframe, their amplitudes are different, leading to a different weighting of field configurations when computing ensemble averages such as in equation (14). It is therefore important to investigate this possible shortcoming further in this Appendix.

A1 More realistic spin proxies and peak

For this purpose, one can in principle (i) impose an additional peak constraint at the location where the spin is computed in order to impose that a protohalo will form there, and (ii) use more realistic spin proxies.

The peak constraint will typically be at a smaller scale than the filament's constraint, which requires building a two-scale theory and therefore increases significantly the complexity of the formalism. An additional difficulty with (ii) is that standard local proxies for the inertia tensor are highly non-linear and therefore require high-dimensional *numerical* integrations that are fairly difficult to implement in practice. For instance, considering the proxy that Schäfer & Merkel (2012) use to locally approximate the inertia tensor, we have

$$I_{ij} = \frac{M}{5} \begin{pmatrix} A_y^2 + A_z^2 & 0 & 0 \\ 0 & A_z^2 + A_x^2 & 0 \\ 0 & 0 & A_x^2 + A_y^2 \end{pmatrix}, \quad (\text{A2})$$

(in the frame of the Hessian) where the mass is $M = 4/3\pi A_x A_y A_z \rho_0 a_0^3$ and the semi-axes of the ellipsoid, A_i , are function of the eigenvalues of the Hessian (negative for a peak),

$$A_i = \sqrt{\frac{2\nu\sigma_2}{-\lambda_i}}. \quad (\text{A3})$$

The traceless part of I_{ij} that is relevant for torques is then proportional to the traceless part of the inverse Hessian

$$\bar{I}_{ij} = \frac{2}{5} \nu \sigma_2 M \bar{H}_{ij}^{-1}. \quad (\text{A4})$$

This introduces singular factors like $1/\sqrt{\det \mathbf{H}}$ in the expectation for $\langle s \rangle$. Such factors make the numerical evaluation of equation (24) more challenging as discussed in Section 2. We therefore postpone their evaluation in three dimensions to future work. Let us briefly investigate their implementation in two dimensions. In Appendix A2, we introduce a multiscale description while in Appendix A3 we take into account the proxy given by equation (A2) and we add an explicit peak condition.

A2 A 2D multiscale analysis

The evaluation of r_* , see equation (20), requires to look for the scale that maximizes the spin amplitude. An improvement to the main text's approach is to investigate this issue in a two-scale theory where the scale of the central peak is larger than the scale of the halo. In this section, we propose to describe how to implement this multiscale theory and we show that this more accurate multiscale estimate for r_* yields, following the main text, a very similar value for the critical mass.

More specifically, let us smooth the fields in \mathbf{r}_Y (the location of the spin) on R_h , an additional parameter, characterizing the halo's size and the fields in \mathbf{r}_X on a different scale $R_s > R_h$ in order to impose a large-scale filament (a peak in 2D). If the one-point covariance matrix \mathbf{C}_0 , does not change for a power-law power spectrum, the two-point covariance matrix \mathbf{C}_Y does. In particular, all correlation functions ξ are now function of r , R_s and R_h . For instance for a power-law density power spectrum, $P(k) \propto k^n$,

$$\xi_{\phi\phi}^{\Delta\Delta}(r) = \left(\frac{R_s^2 + R_h^2}{2R_s R_h} \right)^{-\frac{n+2}{2}} \left[\mathcal{F}_1^2 - \frac{1}{8}(n+2) \frac{r^2}{R_s^2 + R_h^2} \mathcal{F}_2^3 \right],$$

where $\mathcal{F}_i^j = {}_1F_1(n/2 + i; j; -r^2/2(R_s^2 + R_h^2))$. The mean spin in \mathbf{r}_Y is then given by the expectation of $\tilde{s}_z = \sum_{i,j,k} \epsilon_{ij3} \phi_{ik} x_{jk}$ given a peak on scale R_s in \mathbf{r}_X as was computed in the main text. Compared to the main text, the only difference here is that we now also take into account the two-scale process through the two smoothing scales, R_s and R_h . The maximum spin magnitude as a function of the scale R_s/R_h is then computed and displayed in Fig. A1. It appears that the spin magnitude is non-monotonic, peaking at $R_h = 0.8R_s$ which is very close to the value of $r_* \approx 0.7R_s$ (when top-hat smoothing are taken for both lengths).

Note that as we are computing here only the component of the spin along the filament, our magnitude plot does not contain the mass pre-factor, and our proxy for the moment of inertia, $\mathbf{I} \approx \mathbf{H}$, reflects only its orientation, but not its magnitude. We are able to argue, however,

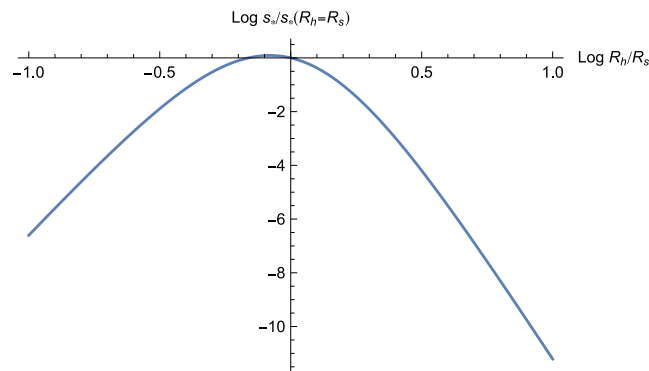


Figure A1. Maximum of spin as a function of the halo's scale R_h .

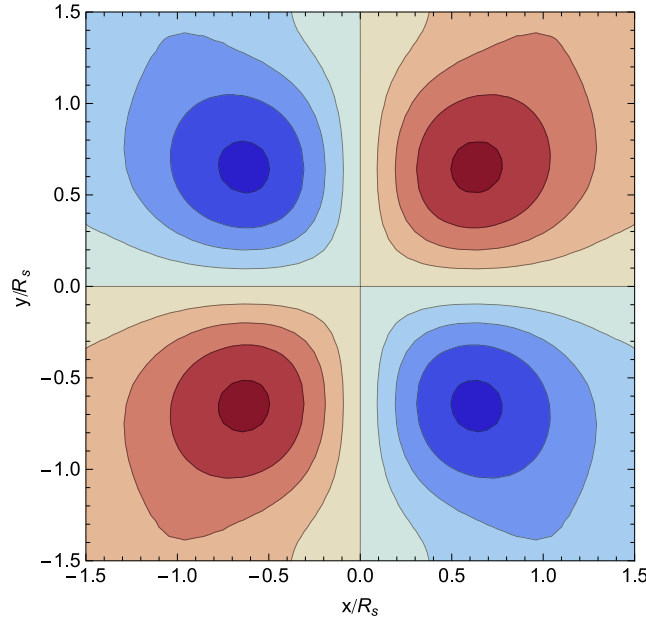


Figure A2. Mean spin computed via numerical integrations when (i) a central peak with geometry given by $\nu = 1$, $\lambda_1 = -1$, $\lambda_2 = -2$ is set, (ii) the inertia tensor is approximated by equation (A2), (iii) the scale of the central peak R_s is different from the scale of the halo R_h (here we take $R_h/R_s = 1/10$), (iv) there is a peak constraint at the location where the spin is computed with height $\nu = 5/2$, negative eigenvalues and zero gradient. The density power spectrum is a power law here with spectral index $n = 1/2$.

that Fig. A1 displays a maximum spin alignment with the filament’s direction for some critical value of R_h – as it shows first an increase and then a fall in the z -component of the spin that is due to Hessian-tidal shear alignment.

A3 A 2D multiscale analysis with peak constraint

Adding a peak constraint at the location of the spin and taking into account the proxy given by equation (A2) is more difficult as it requires a numerical integration to account for the sign constraints on the eigenvalues. Notwithstanding this shortcoming, we will show now that in two dimensions, the adjunction of a peak constraint preserves both the qualitative picture (same geometry with four quadrants of opposite spin direction) as well as the typical scale for r_* .

Fig. A2 indeed shows the numerical integration of the mean spin when (i) the inertia tensor is approximated by equation (A4) – where the mass is fixed by the smoothing length R_h –, (ii) the scale of the central peak R_s is different from the scale of the halo R_h (here we take $R_h/R_s = 1/10$), (iii) there is a peak constraint at the location where the spin is computed with height $\nu = 5/2$, negative eigenvalues and zero gradient. In short, the mean spin is now computed as

$$\langle \tilde{s} | \text{pk}, \text{pk} \rangle = \frac{\langle \tilde{s} \det[\mathbf{H}] \Theta(-\lambda_i) \delta_D(x - \nu) \delta_D(x_i) | \text{pk} \rangle}{\langle \det[\mathbf{H}] \Theta(-\lambda_i) \delta_D(x - \nu) \delta_D(x_i) | \text{pk} \rangle}, \quad (\text{A5})$$

where \tilde{s}_i is defined as $\tilde{s}_i = \sum_{j,k,l} \epsilon_{ijk} H_{jl}^{-1} T_k$ while the expectations $\langle \cdot | \text{pk} \rangle$ are defined as conditional expectation to a central peak of geometry $\nu = 1$, $\lambda_1 = -1$, $\lambda_2 = -2$. The mean spin map is then obtained by numerical integration. Fig. A2 clearly shows that the four quadrants of opposite spin direction, as well as the size of these quadrants are preserved. This test strongly suggests that in two dimensions, improvements beyond the $\mathbf{I} \approx \mathbf{H}$ approximation do not change the global picture described in the main text.

Further developments, beyond the scope of this paper, could be to carry out the same analysis in three dimensions, also adding a peak constraint at the location where the spin is computed in order to impose the existence of a protohalo and use equation (A2) to define its inertia tensor. While the two-scale analysis is straightforward enough to implement, the adjunction of a peak constraint in three dimensions is much more tricky and requires in particular the computation of high-dimension numerical integrals (the results will not be analytic anymore) that are left for future investigations.

APPENDIX B: DUAL VOID THEORY

The theory presented in Section 4.1 is algebraic. Effectively no assumption has been made about the signs of the eigenvalues of the saddle we are considering. It is therefore also perfectly valid in the neighbourhood of a wall-type saddle in order to describe the spin alignments of dark haloes in that vicinity. At a qualitative level, Fig. 3 applies up to a sign: voids and wall saddles repel. It follows that the spins should rotate around the wall saddle to void axis and become parallel near the wall with a point symmetric change of polarity. This is indeed what equation (25) predicts and is shown on Fig. B1.

The statistical significance of these alignments is likely to be reduced as there are much fewer galaxies in voids and near wall saddles.

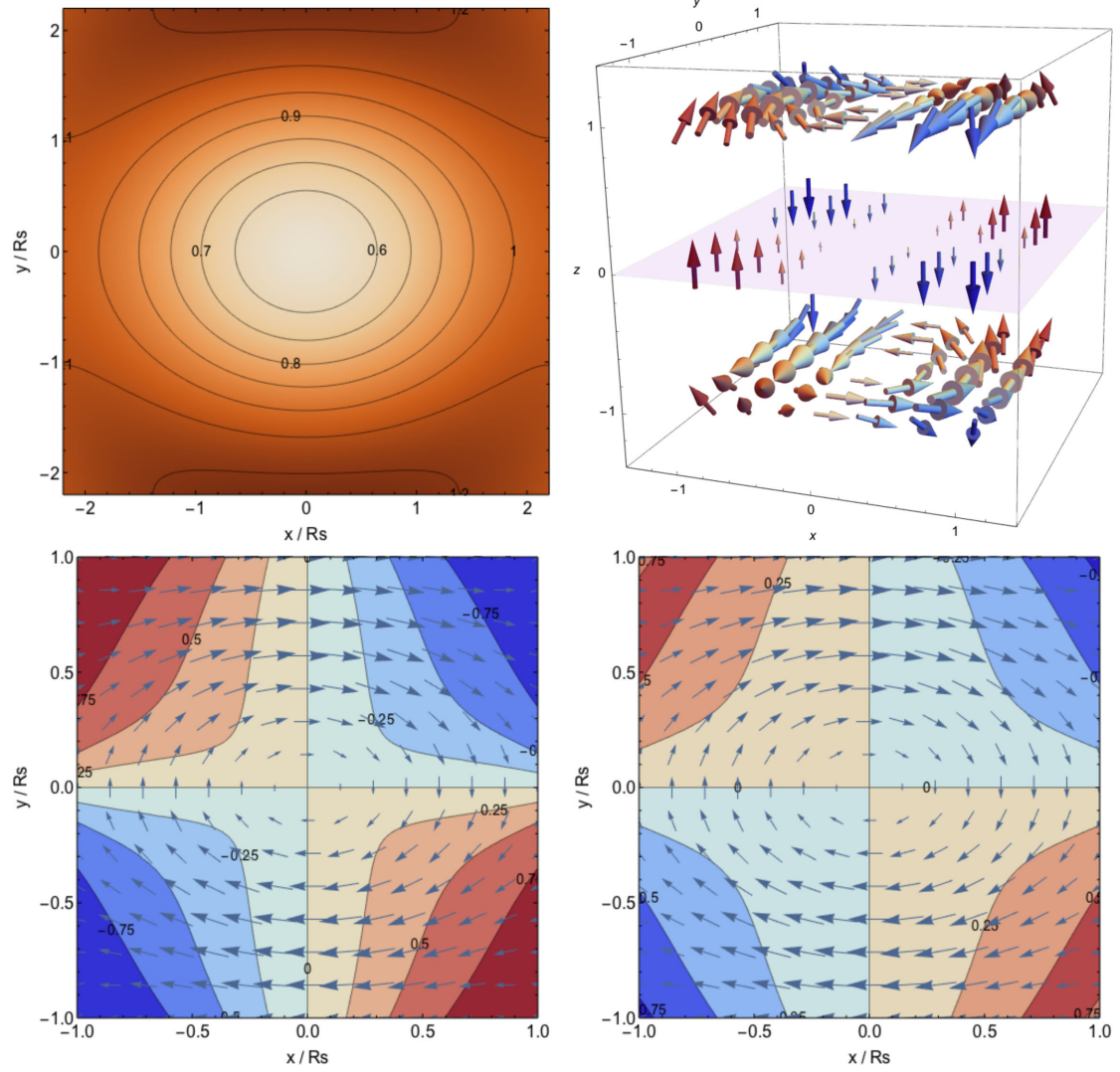


Figure B1. Top left-hand panel: mean density in the plane of the wall Oxy and centred on a wall-type filament with geometry $\nu = 0.5$, $\lambda_1 = 0.8$ along the x -axis, $\lambda_2 = 0.6$ along the y -axis and $\lambda_3 = -0.5$ along the z -axis for a power-law density power spectrum with spectral index $n = -2$. Contours are displayed from $\delta = 0.6$ to 1.2 as labelled. The filaments are clearly seen around $y = \pm 2R_s$. Top right-hand panel: mean spin colour coded by its projection along the normal to the wall. The spins are aligned with the normal in the plane of the wall and perpendicular to it when going outside the plane of the wall. Bottom panels: mean spin vectors at $z = 0.5R_s$ (left) and $z = 1R_s$ (right). Contours represent the orientation of the spin with regards to the normal to the wall from -1 (anti-aligned, red) to $+1$ (aligned, blue) through 0 (perpendicular).

APPENDIX C: TECHNICAL COMPLEMENTS

C1 Codes for density and spin in 2/3D

The expression for the 2 and 3D spin statistics (mean and variance) for scale-invariant power spectra are available both as a mathematica package (<http://www.iap.fr/users/pichon/spin/code/ATTT.m>), and a mathematica notebook (<http://www.iap.fr/users/pichon/spin/code/ATTT-package.nb>). The following functions are provided: $\delta 2D$, $\text{spin}2D$, $\text{var}2D$, $\delta 3D$, $\text{spin}3D$, which correspond, resp. to the 2D density, spin, its variance, and in 3D the density and the spin for scale-invariant power spectra of index n as a function of position r , θ , (ϕ) and the geometry of the peak (resp. saddle) ν , λ_1 , λ_2 , (λ_3) . Compiled versions are also provided.

C2 Correlation functions for power-law spectra

The 2D correlation functions defined in equations (5) and (9) can be analytically obtained for density power-law power spectrum $P_k(k) \propto k^n$ for which the scale parameter is $\gamma = \sqrt{(n+2)/(n+4)}$:

$$\xi_{\phi\phi}^{\Delta\Delta}(r) = \mathcal{F}_1^2 - \frac{1}{16}(n+2)r^2\mathcal{F}_2^3,$$

$$\begin{aligned}
\xi_{\phi x}^{\Delta\Delta}(r) &= \gamma \left(\frac{(n+4)}{16} r^2 \mathcal{F}_3^3 - \mathcal{F}_2^2 \right), \\
\xi_{xx}^{\Delta\Delta}(r) &= \mathcal{F}_3^2 - \frac{1}{16} (n+6) r^2 \mathcal{F}_4^3, \\
\xi_{\phi\phi}^{\Delta+}(r) &= -\frac{1}{32} (n+2) r^2 \mathcal{F}_2^3, \\
\xi_{\phi x}^{\Delta+}(r) &= \frac{\gamma}{32} (n+4) r^2 \mathcal{F}_3^3, \\
\xi_{xx}^{\Delta+}(r) &= -\frac{1}{32} (n+6) r^2 \mathcal{F}_4^3, \\
\xi_{\phi\phi}^{\times\times}(r) &= \frac{1}{8} (4\mathcal{F}_1^2 - 3\mathcal{F}_1^3), \\
\xi_{\phi x}^{\times\times}(r) &= -\frac{\gamma}{8} (4\mathcal{F}_2^2 - 3\mathcal{F}_2^3) \\
\xi_{xx}^{\times\times}(r) &= \frac{1}{8} (4\mathcal{F}_3^2 - 3\mathcal{F}_3^3),
\end{aligned} \tag{C1}$$

where r is in units of the smoothing length and $\mathcal{F}_i^j = {}_1F_1(n/2 + i; j; -r^2/4)$, with ${}_1F_1$ the Hypergeometric functions of the first kind. Some of those correlation functions are plotted in Fig. 5.

The 3D correlation functions can similarly be obtained for power-law power spectrum $P_k(k) \propto k^n$ (some of those correlations are plotted in Fig. 10) for which the scale parameter is $\gamma = \sqrt{(n+3)/(n+5)}$ and we define $\mathcal{G}_i^j = {}_1F_1(n + i/2; j/2; -r^2/4)$:

$$\begin{aligned}
\xi_{\phi\phi}^{\Delta\Delta}(r) &= \frac{-32(n-1)\mathcal{G}_1^3 - ((2-4n)r^2 + r^4 - 32)\mathcal{G}_{-1}^1 + (n-2)(2nr^2 - r^4 + 32)\mathcal{G}_{-1}^3}{2(n^2-1)r^2}, \\
\xi_{\phi x}^{\Delta\Delta}(r) &= \frac{\Gamma\left(\frac{n+1}{2}\right)(32(n+1)\mathcal{G}_3^3 + (-2(2n+3)r^2 + r^4 - 32)\mathcal{G}_1^1 + n(-2(n+2)r^2 + r^4 - 32)\mathcal{G}_1^3)}{8r^2\sqrt{\Gamma\left(\frac{n+3}{2}\right)}\sqrt{\Gamma\left(\frac{n+7}{2}\right)}}, \\
\xi_{xx}^{\Delta\Delta}(r) &= \frac{-32(n+3)\mathcal{G}_5^3 + (2(2n+7)r^2 - r^4 + 32)\mathcal{G}_3^1 + (n+2)(2(n+4)r^2 - r^4 + 32)\mathcal{G}_3^3}{2(n+3)(n+5)r^2}, \\
\xi_{\phi\phi}^{\Delta+}(r) &= \frac{(4n(r^2+3) - (r^2+8)r^2 - 40)\mathcal{G}_{-1}^1 + 16(n-1)\mathcal{G}_1^3 + (n-2)(2(n-3)r^2 - r^4 - 28)\mathcal{G}_{-1}^3}{2(n^2-1)r^2}, \\
\xi_{\phi x}^{\Delta+}(r) &= \frac{\Gamma\left(\frac{n+1}{2}\right)(-16(n+1)\mathcal{G}_3^3 + (-4n(r^2+3) + r^4 + 16)\mathcal{G}_1^1 + n(-2(n-1)r^2 + r^4 + 28)\mathcal{G}_1^3)}{8r^2\sqrt{\Gamma\left(\frac{n+3}{2}\right)}\sqrt{\Gamma\left(\frac{n+7}{2}\right)}}, \\
\xi_{xx}^{\Delta+}(r) &= \frac{16(n+3)\mathcal{G}_5^3 + (4(n+2)r^2 + 12n - r^4 + 8)\mathcal{G}_3^1 + (n+2)(2(n+1)r^2 - r^4 - 28)\mathcal{G}_3^3}{2(n+3)(n+5)r^2}, \\
\xi_{\phi\phi}^{\times\times}(r) &= \frac{((n-2)r^2(r^2+10) - 48)\mathcal{G}_{-1}^3 + (-2(n-6)r^2 + r^4 + 48)\mathcal{G}_{-1}^1}{(n^2-1)r^4}, \\
\xi_{\phi x}^{\times\times}(r) &= -\frac{\Gamma\left(\frac{n+1}{2}\right)((nr^2(r^2+10) - 48)\mathcal{G}_1^3 + (-2(n-4)r^2 + r^4 + 48)\mathcal{G}_1^1)}{4r^4\sqrt{\Gamma\left(\frac{n+3}{2}\right)}\sqrt{\Gamma\left(\frac{n+7}{2}\right)}}, \\
\xi_{xx}^{\times\times}(r) &= \frac{((n+2)r^2(r^2+10) - 48)\mathcal{G}_3^3 + (-2(n-2)r^2 + r^4 + 48)\mathcal{G}_3^1}{(n+3)(n+5)r^4}.
\end{aligned}$$

C3 Correlation functions for LCDM spectra

The same ξ correlation functions can also be computed for a Λ CDM power spectrum using Bardeen et al. (1986) and equation (9). The corresponding functions are shown on Fig. C1 for a Gaussian smoothing length of $R_s = 5\text{Mpc } h^{-1}$ and a WMAP-7 cosmology. Note that those correlation functions are quite similar to $n = -2$ power-law power spectrum (see Fig. 10). Given these correlations, it would be straightforward to compute the corresponding spin.

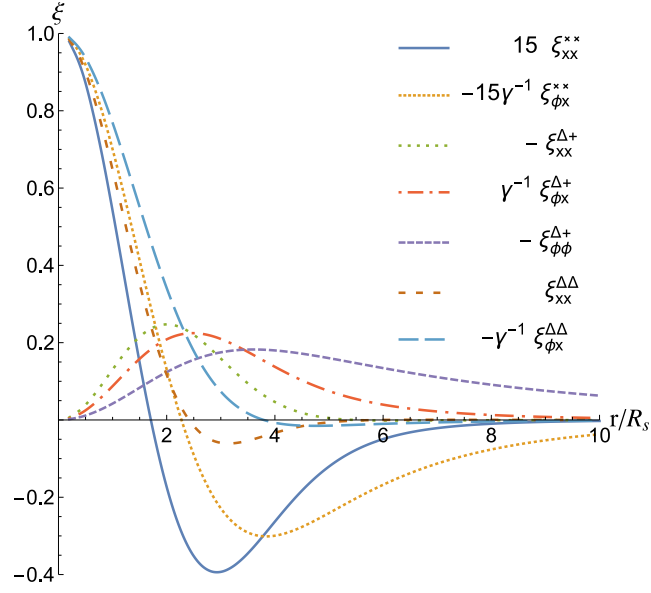


Figure C1. Two-point correlation functions as a function of the separation r in units of the smoothing length $R_s = 5 \text{ Mpc } h^{-1}$ for a Λ CDM power spectrum.

This paper has been typeset from a $\text{\TeX}/\text{\LaTeX}$ file prepared by the author.